
STRUCTURALLY ADAPTIVE MULTI-DERIVATIVE REGULARIZATION FOR IMAGE RECOVERY FROM SPARSE FOURIER SAMPLES

A PREPRINT

Sanjay Viswanath, Manu Ghulyani, and Muthuvel Arigovindan*

Imaging Systems Lab
Department of Electrical Engineering
Indian Institute of Science (IISc)
Bangalore 560012, India

June 29, 2021

ABSTRACT

The importance of regularization has been well established in image reconstruction—which is the computational inversion of imaging forward model—with applications including deconvolution for microscopy, tomographic reconstruction, magnetic resonance imaging, and so on. Originally, the primary role of the regularization was to stabilize the computational inversion of the imaging forward model against noise. However, a recent framework pioneered by Donoho and others, known as compressive sensing, brought the role of regularization beyond the stabilization of inversion. It established a possibility that regularization can recover full images from highly undersampled measurements. However, it was observed that the quality of reconstruction yielded by compressive sensing methods falls abruptly when the under-sampling and/or measurement noise goes beyond a certain threshold. Recently developed learning-based methods are believed to outperform the compressive sensing methods without a steep drop in the reconstruction quality under such imaging conditions. However, the need for training data limits their applicability. In this paper, we develop a regularization method that outperforms compressive sensing methods as well as selected learning-based methods, without any need for training data. The regularization is constructed as a spatially varying weighted sum of first- and canonical second-order derivatives, with the weights determined to be adaptive to the image structure; the weights are determined such that the attenuation of sharp image features—which is inevitable with the use of any regularization—is significantly reduced. We demonstrate the effectiveness of the proposed method by performing reconstruction on sparse Fourier samples simulated from a variety of MRI images.

Keywords Adaptive Regularization, Total Variation, Magnetic Resonance Imaging, Image Reconstruction

1 Introduction

Magnetic resonance imaging (MRI) is one of the important medical imaging modalities in modern medicine for both clinical practice and medical research. Its importance stems from the fact that it is absolutely non-invasive. An MRI system measures samples of the Fourier transform of a cross-sectional plane of interest [1, 2]. The measured samples in the Fourier plane typically lie on a trajectory that is determined by the physical constraints of the imaging system. In most systems, the measured samples are transformed into a set of samples on a cartesian grid via interpolation, such that the required real space image is obtained by simple inverse discrete Fourier transform [1, 2]. However, this type of image reconstruction method leads to serious artifacts, when the measured Fourier samples are not sufficiently dense. A dense sampling is impractical in cases where it is required to reduce the scan time [3]. In such cases, the method

*Corresponding author (mvel@iisc.ac.in)

of compressive sensing, pioneered by Donoho and others [4–13], becomes a better alternative [3, 14–20], as it can reconstruct good quality images from sparse samples. Unlike direct inversion, the method of compressive sensing formulates the reconstruction problem as an inverse problem and solves it by employing numerical optimization as given in Figure 1. In this scheme, a cost function composed of the following parts is constructed:

- A data error term that measures the goodness of fit of the candidate image to the measured data through the imaging forward model, which can be expressed as

$$F(s, \mathbf{m}, T) = \|Ts - \mathbf{m}\|_2^2, \quad (1)$$

where T represents a sampling operator in the Fourier domain that returns a vector of complex Fourier samples from the candidate image s , \mathbf{m} denotes the vector of measured samples, and $\|\cdot\|_2$ represents the magnitude of its vector/matrix argument which is the square root of the sum of squares of its elements.

- An image regularization cost $R(s)$, that measures the overall roughness of the candidate image through image derivatives. The most commonly used forms for $R(s)$ are given below [21–23]:

$$R_1(s) = \sum_{\mathbf{r}} \|\nabla s(\mathbf{r})\|_2, \quad (2)$$

$$R_2(s) = \sum_{\mathbf{r}} \|\nabla^2 s(\mathbf{r})\|_F, \quad (3)$$

$$R_{hs}(s) = \sum_{\mathbf{r}} \|\nabla^2 s(\mathbf{r})\|_{S(1)}, \quad (4)$$

where ∇ and ∇^2 are gradient and Hessian operators. The symbols $\|\cdot\|_2$ and $\|\cdot\|_F$ denotes vector and matrix norms that are computed as the square root of the sum of squares of the elements. The symbol $\|\cdot\|_{S(1)}$ denotes the Nuclear-norm, which is the sum of modulus of Eigenvalues of its matrix argument. $R_{hs}(s)$ has proven to be one of the best performing regularizations.

The numerical optimization program evaluates a weighted sum of the form $J(s, \mathbf{m}, T, \lambda) = F(s, \mathbf{m}, T) + \lambda R(s)$ where λ is the user-defined weight determining the trade-off between the data error and the image roughness. This cost is evaluated along with its gradient for a series of candidates images (varying $s(\mathbf{r})$), and determines the minimum, which becomes the required reconstructed image $s^*(\mathbf{r})$. We will denote this operation by

$$s^* = \mathcal{M}(\text{Data} = \{T, \mathbf{m}\}, \lambda). \quad (5)$$

In the figure, the symbol, $\hat{s}(\mathbf{r})$ denotes the initialization required for the numerical optimization. Regularized reconstruction methods that use the forms of regularization given in the equations (2), (3), and (4) are also called total variation (TV) methods. We will refer to this type of methods as the derivative-based regularization methods. Further developments in derivative-based regularization include total generalized variation (TGV) [24], which is believed to give superior reconstruction. A detailed overview of such methods has been provided in the supplementary material. It has been observed that compressive sensing methods also give reconstruction artifacts, when the sampling is very sparse and/or noise is very high. In recent years, there has been increased focus on developing deep learning based methods [25–32], since it is generally believed that such methods do not produce artifacts in the reconstruction. This belief is based on the following fact: while regularization methods impose ad hoc prior models on the image characteristics, deep-learning methods encompass natural prior information derived from training data. However, deep learning-based methods require training data in the form of thousands of image pairs, where each pair contains a typical measured image and the corresponding ground-truth image that might have generated the measurement. Such a requirement limits the applicability of deep learning based methods. Furthermore, stability issues have also been reported in such deep learning methods for image reconstruction [33].

Our goal here is to develop a novel type of reconstruction method that has the desirable traits of both deep-learning and derivative-based regularization methods. In other words, our interest is to develop a method that neither results in a significant amount of distortions under the conditions of severe noise and under-sampling, nor requires any training data. To brief the concepts involved in our approach, we first need to understand why derivative-based regularization methods give distortions in the reconstructions when noise or under-sampling is severe. To this end, we first note that employing derivatives in regularization has the following desirable effects: (i) minimizing derivative magnitudes summed over pixels leads to sparse distribution of large derivatives in the reconstruction, which results in the elimination of noise; (ii) additionally, in the case of MRI reconstruction, minimizing derivative magnitudes counter-acts with oscillations caused by under-sampling in Fourier space, thereby leading to the interpolation of lost Fourier samples. However, minimizing derivative has also an undesirable effect: as high-resolution image features will have high derivative values, using derivative-based regularization inevitably leads to distortions that cause some loss of resolution. Our goal is to build an

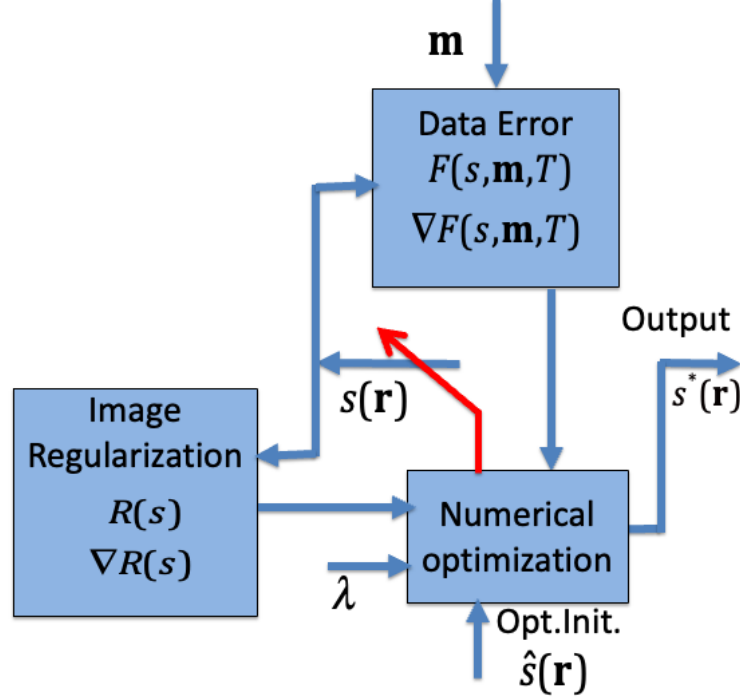


Figure 1: Schematic of regularized image reconstruction. \mathbf{m} denotes the measured data. $F(s, \mathbf{m}, T)$ represents the data error with T denoting the measurement model of the imaging system. $R(s)$ is the measure of image roughness (regularization). $\nabla F(s, \mathbf{m}, T)$ and $\nabla R(s)$ represent gradients of $F(s, \mathbf{m}, T)$ and $R(s)$ respectively, which are required for the numerical optimization. λ is the user parameter that determines the trade-off between data error and image roughness.

improved derivative-based regularization scheme with the following property: it should have a reduced penalizing effect on the derivatives that are part of the image structure without losing its penalizing effect on the derivatives originating from noise and oscillations. We call such property structural adaptivity. Such a regularization method with structural adaptivity will hopefully have the desirable traits: it will not give significant amount of distortion under severe noise and under-sampling, and it will not require training data.

To build a regularization scheme with structural adaptivity, we draw inspiration from the human visual system. It is a well-known fact that the human visual system can localize object boundaries in the presence of a very large amount of noise because of its inherent ability to process images simultaneously at multiple resolutions [34, 35]. Because of this ability, the human visual system can discriminate sharp jumps in the intensity that is part of an object boundary against sharp jumps caused by noise. Inspired by the ability of the human visual system, we build our structural adaptive regularization in the form of a multiresolution scheme. We do this by constructing a series of reconstruction modules with progressively increasing target resolutions, where the reconstruction from a module with lower target resolution serves as a guide for building the adaptive regularization for the module with a higher target resolution. This leads to two questions: how to define the adaptive regularization, given a guide image, and how to define modules with progressively increasing target resolution. The first question is answered in Section 2, and the second question is answered in Section 3. These sections only deal with the main concepts involved in our method. The optimization tools necessary for the practicable realization of our method are developed in the supplementary Sections E and F, and these also constitute our important technical contributions.

In Section 4 we present an extensive set of reconstruction results and demonstrate that the proposed method outperforms all derivative-based regularization methods, and prominent deep learning methods. The key factor that makes our methods superior to deep learning methods and other regularization methods is that the adaptive regularization does not penalize high images derivatives that are part of the image structures; this is in contrast with standard regularization methods, which are unable to discriminate derivatives that are part of the structures against derivatives originating from noise. This is made possible by the structural adaptivity resulting from the multiresolution scheme that we propose. The idea of multi-resolution has been extensively used for other processing tasks such as image registration [36–38], and image segmentation [39–41] with strong inspiration derived from the way the human visual system operates [34, 35].

However, the power of multiresolution has not been used for gaining robustness in image reconstruction so far, and the present work uses the power of multiresolution for the first time. The method that we develop here is an extension of the method we recently published called Combined Order Regularization with Optimal Spatial Adaptation (COROSA) [42].

2 The basic adaptive regularized reconstruction

As explained before, our multiresolution-based adaptive regularization scheme will be in the form of a series of reconstruction modules; each module performing an adaptive regularized reconstruction by using the information from the guide image, which is obtained as the reconstruction from the previous module. Obviously, the key to the success of this scheme is the construction of a basic adaptive regularized reconstruction module that can extract information for structural adaptation from the guide image. To this end, we make use of the following observation: the relative spatial distribution of the image gradient and the Eigenvalues of image Hessian has important information about the image structure. We propose to exploit this towards constructing an adaptive regularization that has the ability to discriminate derivatives that are part of the structures against the derivatives that originate from noise (structural adaptivity). The regularization is constructed as a spatially varying weighted sum of the above-mentioned three terms. The weights are determined adaptively using the guide image such that the resulting regularization has the desired structural adaptivity. We do this in this section in three stages. In Section 2.1, we describe the basic building blocks to be used in adaptive regularization. Next, we develop the adaptive regularized reconstruction method using these building blocks in Section 2.2, and in Section 2.3 we develop a method to extract the information for adaptation from a given guide image.

2.1 Gradient and canonical second derivatives

For a continuous domain function $p(\mathbf{r})$, its gradient denoted by $\nabla p(\mathbf{r})$ is a vector function of the form $\nabla p(\mathbf{r}) = \left[\frac{\partial}{\partial x} p(\mathbf{r}) \quad \frac{\partial}{\partial y} p(\mathbf{r}) \right]^T$. We use the same notation to denote the discrete gradient of a discrete image $s(\mathbf{r})$, i.e., we write $\nabla s(\mathbf{r}) = [(d_x * s)(\mathbf{r}) \quad (d_y * s)(\mathbf{r})]^T$, where $*$ denotes convolution, and, $d_x(\mathbf{r})$ and $d_y(\mathbf{r})$ are the filters implementing discrete equivalents of the first order-derivatives, $\frac{\partial}{\partial x}$, and $\frac{\partial}{\partial y}$ respectively. Summing this gradient magnitude over all pixels of the image $s(\mathbf{r})$ gives the first-order total variation regularization of equation (2).

For a continuous domain function, $p(\mathbf{r})$, the elementary second derivative operators are given by $\mathcal{D}_{xx}p(\mathbf{r}) = \frac{\partial^2}{\partial x^2} p(\mathbf{r})$, $\mathcal{D}_{yy}p(\mathbf{r}) = \frac{\partial^2}{\partial y^2} p(\mathbf{r})$, and $\mathcal{D}_{xy}p(\mathbf{r}) = \frac{\partial^2}{\partial x \partial y} p(\mathbf{r})$. The Hessian is given by $\nabla^2 p(\mathbf{r}) = \begin{bmatrix} \mathcal{D}_{xx}p(\mathbf{r}) & \mathcal{D}_{xy}p(\mathbf{r}) \\ \mathcal{D}_{xy}p(\mathbf{r}) & \mathcal{D}_{yy}p(\mathbf{r}) \end{bmatrix}$. The Eigenvalues of Hessian are given by

$$\mathcal{H}^+ p(\mathbf{r}) = \frac{1}{2} (\mathcal{L}p(\mathbf{r}) + \mathcal{C}p(\mathbf{r})), \quad (6)$$

$$\mathcal{H}^- p(\mathbf{r}) = \frac{1}{2} (\mathcal{L}p(\mathbf{r}) - \mathcal{C}p(\mathbf{r})), \quad (7)$$

where

$$\mathcal{C}p(\mathbf{r}) = \sqrt{(\mathcal{D}_{xx}p(\mathbf{r}) - \mathcal{D}_{yy}p(\mathbf{r}))^2 + 4\mathcal{D}_{xy}p(\mathbf{r})}, \quad (8)$$

and $\mathcal{L}p(\mathbf{r})$ is the well-known Laplacian operator given by $\mathcal{L}p(\mathbf{r}) = \mathcal{D}_{xx}p(\mathbf{r}) + \mathcal{D}_{yy}p(\mathbf{r})$. For brevity, we call these Eigenvalues, the canonical second derivatives (CSDs). The term ‘‘canonical’’ is justified because of the following reasons: (i) these quantities themselves are second derivative taken along the directions that make angles $\theta(\mathbf{r})$ and $\theta(\mathbf{r}) + \pi/2$ with the x -axis, where $\theta(\mathbf{r})$ is the \mathbf{r} -dependent angle determined by the elementary derivatives $\mathcal{D}_{xx}p(\mathbf{r})$, $\mathcal{D}_{yy}p(\mathbf{r})$, and $\mathcal{D}_{xy}p(\mathbf{r})$; (ii) any second derivative taken along a direction that makes an arbitrary angle, ϑ , can be expressed as $\mu\mathcal{H}^+ p(\mathbf{r}) + (1 - \mu)\mathcal{H}^- p(\mathbf{r})$ where μ is a real number in the range $[0, 1]$ that is determined by the angle ϑ ; (iii) these quantities are invariant with respect to rotations of the image. For a discrete image, $s(\mathbf{r})$, we use the same notations to denote the CSDs, with an understanding that the constituent operators $\mathcal{D}_{xx}s(\mathbf{r})$, $\mathcal{D}_{yy}s(\mathbf{r})$, and $\mathcal{D}_{xy}s(\mathbf{r})$ are implemented by means of discrete convolutions with appropriately designed filters denoted by $d_{xx}(\mathbf{r})$, $d_{yy}(\mathbf{r})$, and $d_{xy}(\mathbf{r})$. In the supplementary material, we have given the implementation of filters d_x , d_y , d_{xx} , d_{yy} , and d_{xy} .

2.2 Adaptive regularized reconstruction

As mentioned before, the most widely used regularizations that are considered to be well-performing are the ones expressed in Equations (2), (3), (4). $R_1(s)$ is constructed by simply summing $\|\nabla s(\mathbf{r})\|_2$ across all pixels. Further,

$R_{hs}(s)$ is constructed by summing $|\mathcal{H}^+s(\mathbf{r})| + |\mathcal{H}^-s(\mathbf{r})|$ across all pixels, whereas, $R_2(s)$ is constructed by summing $\sqrt{(\mathcal{D}_{xx}s(\mathbf{r}))^2 + (\mathcal{D}_{yy}s(\mathbf{r}))^2 + 2(\mathcal{D}_{xy}s(\mathbf{r}))^2}$ across all pixels. It turns out that this is the same as summing $\sqrt{(\mathcal{H}^+s(\mathbf{r}))^2 + (\mathcal{H}^-s(\mathbf{r}))^2}$ across all pixels. In our viewpoint, although these regularizations efficiently remove noise, they have the disadvantage that they do not exploit any pattern in the relative distribution of these quantities. We hypothesize that the quantities $\|\nabla s(\mathbf{r})\|_2$, $\mathcal{H}^+s(\mathbf{r})$, and $\mathcal{H}^-s(\mathbf{r})$, will have some pattern in their spatial distribution, and this can be exploited to reduce the loss of resolution that is normally caused by derivative-based regularizations. To this end, we construct the following regularization:

$$R(s, \hat{\beta}_1, \hat{\beta}_2, \hat{\beta}_3) = \sum_{\mathbf{r}} \left(\hat{\beta}_1(\mathbf{r}) \|\nabla s(\mathbf{r})\|_2 + \hat{\beta}_2(\mathbf{r}) |\mathcal{H}^+s(\mathbf{r})| + \hat{\beta}_3(\mathbf{r}) |\mathcal{H}^-s(\mathbf{r})| \right) \quad (9)$$

where $s(\mathbf{r})$ is the candidate for reconstructed image, and $\hat{\beta}_1(\mathbf{r})$, $\hat{\beta}_2(\mathbf{r})$, and $\hat{\beta}_3(\mathbf{r})$ are adaptive weight images satisfying $\sum_i \hat{\beta}_i(\mathbf{r}) = 1$ and $\hat{\beta}_i(\mathbf{r}) \geq 0, i = 1, 2, 3$. The idea is to choose the weights $\hat{\beta}_1(\mathbf{r})$, $\hat{\beta}_2(\mathbf{r})$, and $\hat{\beta}_3(\mathbf{r})$ appropriately to exploit the pattern in the distribution of $\|\nabla s(\mathbf{r})\|_2$, $\mathcal{H}^+s(\mathbf{r})$, and $\mathcal{H}^-s(\mathbf{r})$. At the same time, because of the constraint, $\sum_i \hat{\beta}_i(\mathbf{r}) = 1$, the penalizing effect on the noise will not be compromised. The proposed image reconstruction using this regularization is demonstrated in the schematic of Figure 2. With given measured samples, \mathbf{m} , adaptive weight images $\hat{\beta}_1(\mathbf{r})$, $\hat{\beta}_2(\mathbf{r})$, and $\hat{\beta}_3(\mathbf{r})$, and regularization weight λ , the numerical optimization module evaluates the image regularization $R(s, \hat{\beta}_1, \hat{\beta}_2, \hat{\beta}_3)$ and data error $F(s, \mathbf{m}, T)$ along with their gradients for a series of candidate images (optimization variable $s(\mathbf{r})$) and determines the empirical minimum of the sum $J(s, T, \mathbf{m}, \lambda) = F(s, T, \mathbf{m}) + \lambda R(s, \hat{\beta}_1, \hat{\beta}_2, \hat{\beta}_3)$. This empirical minimum, $s^*(\mathbf{r})$, is the candidate $s(\mathbf{r})$ that has a modulus of the gradient of the cost $J(s, T, \mathbf{m}, \lambda)$ lower than certain user-defined tolerance. In our proposed scheme, the required adaptive weights are

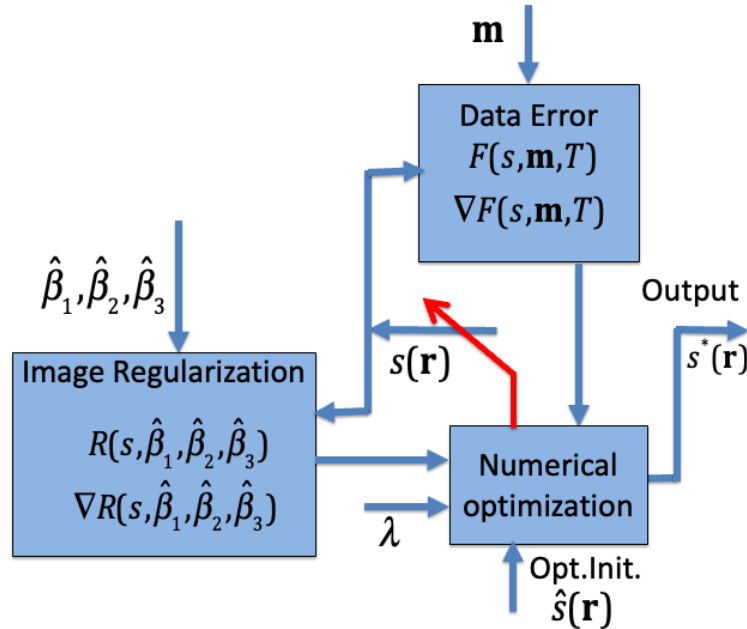


Figure 2: Schematic of adaptive regularized image reconstruction from given adaptive weights

determined from a given guide image $\hat{s}(\mathbf{r})$, that is supplied by the multi-resolution chain to be elaborated in Section 3. We will deal with the issue of finding the adaptive weights $\hat{\beta}_1$, $\hat{\beta}_2$, and $\hat{\beta}_3$ in Section 2.3. A point to be noted is that we will use $\hat{s}(\mathbf{r})$ also for initializing the numerical optimization. It should be emphasized that currently available generic optimization tools are unsuitable for this optimization problem and we develop novel optimization tools for this purpose in the supplementary material. We symbolically denote this numerical optimization based reconstruction operation by

$$s^* = \mathcal{M}_{ad} \left(\text{Init} = \hat{s}, \text{AdapWt} = \{\hat{\beta}_1, \hat{\beta}_2, \hat{\beta}_3\}, \text{Data} = \{T, \mathbf{m}\}, \lambda \right).$$

2.3 Determining the adaptive weights from guide image

We next address the problem of determining the adaptive weights, $\hat{\beta}_1(\mathbf{r})$, $\hat{\beta}_2(\mathbf{r})$, and $\hat{\beta}_3(\mathbf{r})$ from the given guide image $\hat{s}(\mathbf{r})$. We propose to determine these from $\hat{s}(\mathbf{r})$ via minimizing the same regularization cost $R(s, \beta_1, \beta_2, \beta_3)$ w.r.t. $\beta_1(\mathbf{r})$,

$\beta_2(\mathbf{r})$, and $\beta_3(\mathbf{r})$ with the substitution $s(\mathbf{r}) = \hat{s}(\mathbf{r})$. We also impose the constraint that $\beta_1(\mathbf{r}) + \beta_2(\mathbf{r}) + \beta_3(\mathbf{r}) = 1$. The idea behind this approach is that the quantities $\|\nabla s(\mathbf{r})\|_2$, $\mathcal{H}^+ s(\mathbf{r})$ and $\mathcal{H}^- s(\mathbf{r})$ evaluated with substitution $s(\mathbf{r}) = \hat{s}(\mathbf{r})$ will have a pattern that is similar to that of the required reconstruction provided that $\hat{s}(\mathbf{r})$ is a good approximation to the required reconstruction. Hence, the resulting adaptive regularization $R(s, \hat{\beta}_1, \hat{\beta}_2, \hat{\beta}_3)$ to be used in the reconstruction scheme of Figure 2 will have a lesser penalizing effect on the derivatives that confers to the pattern exhibited by guide $\hat{s}(\mathbf{r})$. At the same time, since the constraints, $\sum_i \beta_i(\mathbf{r}) = 1$ and $\beta_i(\mathbf{r}) \geq 0, i = 1, 2, 3$ are imposed, the adaptive regularization $R(s, \hat{\beta}_1, \hat{\beta}_2, \hat{\beta}_3)$ will not have any reduction in the penalizing effect on noise as well as other related artifacts. One technical point is that it is not well-defined to minimize $R(s, \beta_1, \beta_2, \beta_3)$ w.r.t. $\beta_1(\mathbf{r})$, $\beta_2(\mathbf{r})$, and $\beta_3(\mathbf{r})$ because $R(s, \beta_1, \beta_2, \beta_3)$ is linear on $\beta_1(\mathbf{r})$, $\beta_2(\mathbf{r})$, and $\beta_3(\mathbf{r})$. We instead minimize $R(s, \beta_1, \beta_2, \beta_3) + \tau L(\beta_1, \beta_2, \beta_3)$ where $L(\beta_1, \beta_2, \beta_3) = -\sum_{\mathbf{r}} \log(\beta_1(\mathbf{r})\beta_2(\mathbf{r})\beta_3(\mathbf{r}))$. The relevant mathematical explanation for this augmentation with $L(\beta_1, \beta_2, \beta_3)$ is given in the supplementary material. Further, the minimization algorithm is developed in the supplementary material. We denote this minimization operation by

$$(\hat{\beta}_1, \hat{\beta}_2, \hat{\beta}_3) = \mathcal{M}_w(\text{AdapGd} = \hat{s}, \tau). \quad (10)$$

Given the guide image, \hat{s} , process of getting the adaptive weights, $\hat{\beta}_1(\mathbf{r})$, $\hat{\beta}_2(\mathbf{r})$, and $\hat{\beta}_3(\mathbf{r})$ and then the process of obtaining the adaptively regularized reconstruction using $\hat{\beta}_1(\mathbf{r})$, $\hat{\beta}_2(\mathbf{r})$, and $\hat{\beta}_3(\mathbf{r})$ can be represented as a cascade as given below:

$$s^* = \mathcal{M}_{ad}(\text{Init} = \hat{s}, \text{AdapWt} = \mathcal{M}_w(\text{AdapGd} = \hat{s}, \tau), \text{Data} = \{T, \mathbf{m}\}, \lambda). \quad (11)$$

This cascade is represented in Figure 3. This cascade is the basic adaptive regularized reconstruction module to be used for building the multiresolution method. It should be emphasized that, as an adaptation guide, the quality of \hat{s} plays a crucial role in determining the quality of the reconstruction s^* . On the other hand, as an initializer for optimization, the quality of \hat{s} determines the speed of completion of the numerical optimization.

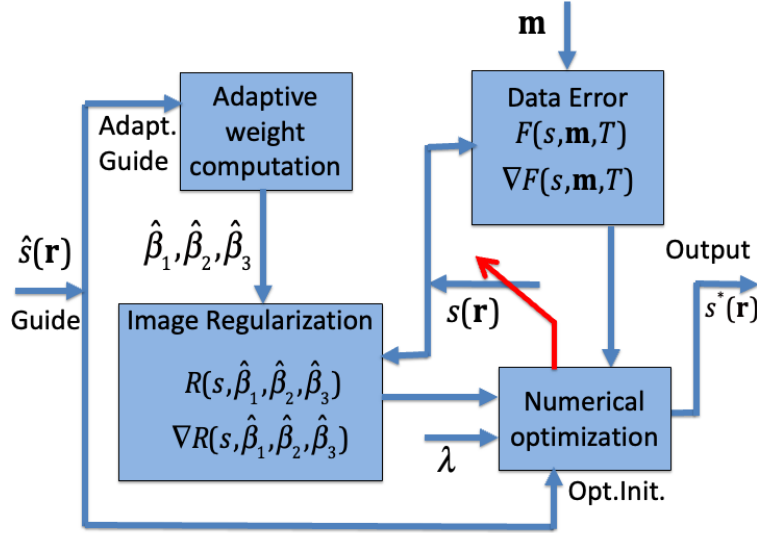
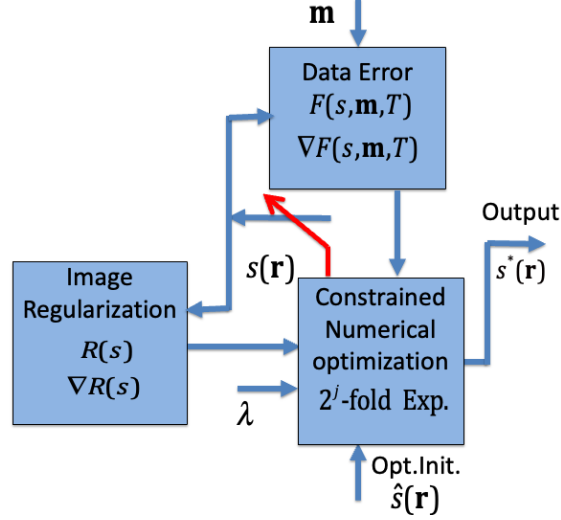
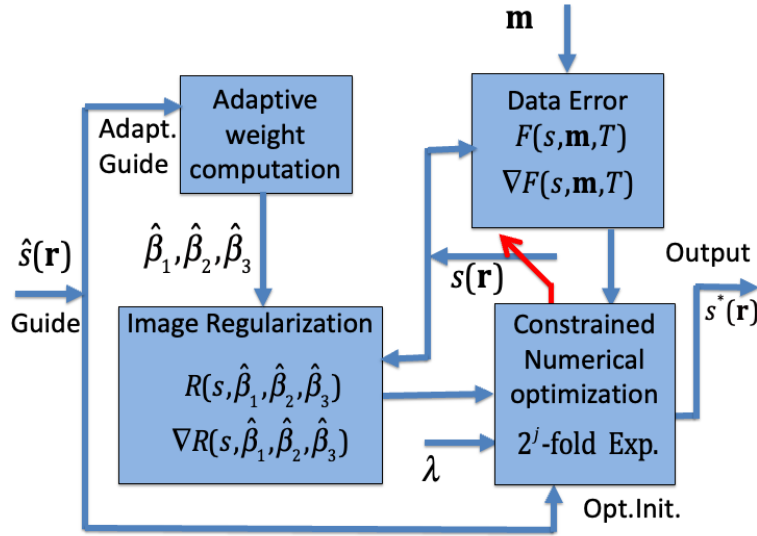


Figure 3: Schematic of adaptive regularized reconstruction from given guide image

3 Multi-resolution based adaptive regularized reconstruction method

Here we build the multiresolution-based adaptive regularized reconstruction method with a progressively increasing resolution by stacking the basic adaptive regularized reconstruction developed in Section 2 (Figure 3). To this end, we introduce the notion of scale- (j) reconstruction. Recall that, in TV regularized reconstruction of Figure 1 and adaptive regularized reconstruction of Figure 3, the numerical optimization module searches for a solution within the space of $N \times N$ images where $N \times N$ is the target image size. In the case of scale- (j) reconstruction, the optimization module searches for the solution within a restricted space of images denoted $\mathcal{S}(N, j)$. Here $\mathcal{S}(N, j)$ denotes space of $N \times N$ images obtained by interpolation from $\frac{N}{2^j} \times \frac{N}{2^j}$ images via a 2^j interpolation. Note that the images in $\mathcal{S}(N, j)$ are 2^j


Figure 4: Schematic of scale-(j) non-adaptive regularized image reconstruction

Figure 5: Schematic of scale-(j) basic adaptive regularized reconstruction

times smoother. The reconstruction operations with this constrained optimization employing non-adaptive and adaptive regularizations are given in Figures 4, and 5 respectively. These reconstruction operations are symbolically represented as follows:

$$s^{(j)} = \bar{\mathcal{M}}^{(j)}(\text{Data} = \{T, \mathbf{m}\}, \lambda) \quad (12)$$

$$s^{(j)} = \bar{\mathcal{M}}_{ad}^{(j)}(\text{Init} = \hat{s}, \text{AdapWt} = \mathcal{M}_w(\text{AdapGd} = \hat{s}, \tau), \text{Data} = \{T, \mathbf{m}\}, \lambda) \quad (13)$$

With this, our multiresolution scheme is constructed as given in Figure 6. The first block labelled as “scale J non-adaptive reconstruction” denotes a reconstruction method where a standard non-adaptive regularization is used (regularization defined in the equation (4)), which is represented by Figure 4 with $j = J$. This is symbolically denoted as

$$s^{(J)} = \bar{\mathcal{M}}^{(J)}(\text{Data} = \{T, \mathbf{m}\}, \lambda). \quad (14)$$

The output $s^{(J)}$ becomes the adaptation guide to the next block, which performs a scale- $(J - 1)$ adaptive regularized reconstruction by searching for the minimum of corresponding adaptive cost within $\mathcal{S}(N, J - 1)$. This block denotes

the reconstruction represented by the schematic of Figure 5 with $j = J - 1$. This operation is represented by

$$s^{(J-1)} = \bar{\mathcal{M}}_{ad}^{(J-1)} \left(\text{Init} = s^{(J)}, \text{AdapWt} = \mathcal{M}_w \left(\text{AdapGd} = s^{(J)}, \tau \right), \text{Data} = \{T, \mathbf{m}\}, \lambda \right). \quad (15)$$

The output $s^{(J-1)}$ becomes the adaptation guide for the scale- $(J-2)$ adaptive regularization reconstruction. This process is continued until the scale-(0) reconstruction is obtained, which can be expressed by the following equation for $j = J-2, \dots, 1, 0$:

$$s^{(j)} = \bar{\mathcal{M}}_{ad}^{(j)} \left(\text{Init} = s^{(j+1)}, \text{AdapWt} = \mathcal{M}_w \left(\text{AdapGd} = s^{(j+1)}, \tau \right), \text{Data} = \{T, \mathbf{m}\}, \lambda \right) \quad (16)$$

These steps are represented by the remaining blocks in Figure 6. The last block, performs scale-(0) adaptive regularized reconstruction, where the optimization block search for the solution within $\mathcal{S}(N, 0)$. Note that $\mathcal{S}(N, 0)$ is the set of $N \times N$ images without any interpolation constraint. In other words, the reconstruction is the same as the one given in Figure 3. This means that the label ‘scale-(0)’ is redundant and hence we skipped it in the last block of Figure 6.

Now, an analysis of this multiresolution scheme is in order. In the series of reconstructions of Figure 6, the first module uses non-adaptive regularization. However, this is not a serious problem, because, the target for this module is a reconstruction that is 2^J smoother than the final reconstruction. Other than this, every reconstruction module receives an adaptation guide that was obtained by another adaptively regularized reconstruction module. Each reconstruction module except the first is able to discriminate high derivative values that are part of the image structure against high derivative values arising from noise and oscillations; this is achieved by making use of the information extracted from the reconstruction output of previous module. Hence, as we proceed through the modules, the resolution of the series of reconstructions, $\{s^{(j)}, j = J-1, J-2, J-3, \dots, 2, 1, 0\}$ improves significantly and becomes better than the resolution that can be obtained by any standard regularization method. In particular, the final reconstruction $s^{(0)}$ will have a significantly improved quality compared to the reconstruction that can be obtained by any standard regularization method.

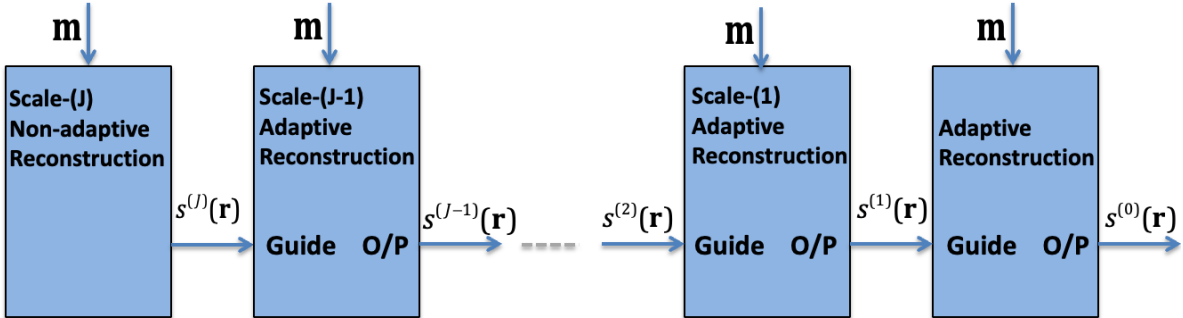


Figure 6: Schematic of multi-resolution based adaptive regularized reconstruction

Now, as the final reconstruction, $s^{(0)}(\mathbf{r})$, will have an improved reconstruction, it can also be used to get improved adaptive weights, $\hat{\beta}_1, \hat{\beta}_2, \hat{\beta}_3$, which in turn, can be used to get a further improved reconstruction by performing an adaptive regularized reconstruction without scale constraint (reconstruction scheme of Figure 3). This argument naturally leads to another series of adaptive regularized reconstructions, where the reconstructed output of one module becomes the adaptation guide for the next module. This can be symbolically expressed, as given below:

$$s_{k+1} = \mathcal{M}_{ad} \left(\text{Init} = s_k, \text{AdapWt} = \mathcal{M}_w \left(\text{AdapGd} = s_k, \tau \right), \text{Data} = \{T, \mathbf{m}\}, \lambda \right). \quad (17)$$

We set $s_0 = s^{(0)}$. Note that the main difference between the series j in the equation (16) and (17) is the following: the reconstructions of the equation (17) work on the final resolution without any interpolation constraint, whereas, the reconstructions of the equation (16) work on gradually increasing resolutions with interpolation constraints. Under certain technical conditions, the above iteration leads to the solution of the following joint minimization problem:

$$(s^*, \beta_1^*, \beta_2^*, \beta_3^*) = \underset{s, \beta_1, \beta_2, \beta_3}{\text{argmin}} F(s, T, \mathbf{m}) + \lambda R(s, \beta_1, \beta_2, \beta_3) + \lambda \tau L(\beta_1, \beta_2, \beta_3) \quad (18)$$

In other words, the sequence $\{s_k\}$ converges to s^* of the above minimization problem. This completes the description of the proposed method. We call our method the Hessian-based combined order regularization with optimal spatial adaptation (H-COROSA). The pre-cursor version, COROSA [42], is obtained by restricting the weights for both canonical second derivatives to be equal.

4 Results

MRI is non-invasive and hence widely adopted in medical diagnosis, and biological investigations. However, there is a serious need to reduce the scan time in MRI to increase the frame rate and avoid motion artifacts. In this viewpoint, we note that an MRI system measures samples of the Fourier transform of a cross-sectional plane along a predefined path determined by the imaging system, and this path is called the sampling trajectory. The fraction of samples measured by the trajectory can be controlled through some parameters, and to reduce the scan time, this fraction has to be kept low. Unfortunately, this leads to serious artifacts if traditional interpolation-based reconstruction methods are used. Recent derivative-based regularization methods (also known as compressive sensing methods), and deep learning based methods, are believed to reduce the artifacts, and the power of such modern methods is measured by their ability to recover sufficient resolution from a low fraction of samples. Further, there is also demand on modern reconstruction methods to recover sufficient resolution from samples with a low signal-to-noise ratio (SNR). This is because low-cost MRI systems have low magnetization strength and hence the measured samples will have low SNR; also, some structures in the imaging specimen may have low magnetizability and hence the measured samples will have low SNR. In this regard, our goal in this section is to study the ability of the proposed regularization to reconstruct images accurately under the conditions of low sampling fraction and high noise in comparison with state-of-the-art regularization methods. Further, we also intend to compare the proposed method with currently popular deep learning-based paradigms. Such deep learning based approaches claim that they do not rely on any ad hoc prior and their claimed performance improvement over regularization methods have made them popular in several fields. At the same time, it is necessary to note that such frameworks require large training sets of appropriate images and they have been observed to be unstable under certain conditions [33]. Nevertheless, it is important to have a perspective on how such methods perform compared to the proposed method.

With these stated objectives, we set up the experiments in two parts: the first part compares H-COROSA with existing derivative-based regularization methods, and the second part deals with the comparison against deep learning based methods. With both sets of experiments, we compare the reconstruction performance using two quantitative scores: Signal to Noise Ratio (SNR) and Structurally Similarity Index (SSIM) [43]. These are widely used in image restoration literature and are useful in the objective evaluation of reconstruction quality. The experimental setup for each set is described in the corresponding subsections below. Before we proceed, we note that sampling fraction is called sampling density in the image reconstruction literature and we will use the same term. Further, in this section, a sampling trajectory with parameters chosen for a specific sampling density is called a sampling scheme.

4.1 Comparison with derivative-based regularization methods

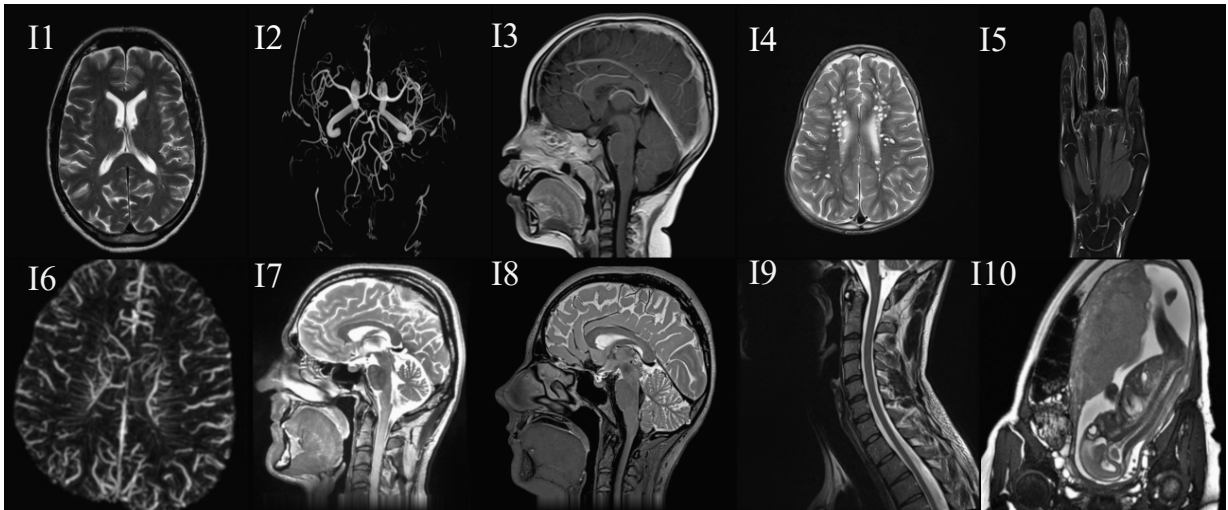


Figure 7: MRI Reference Images I1-I10.

We consider the following regularization methods:

1. Second-order Total Variation (TV2) [21, 22]: this belongs to the class of non-adaptive regularization method depicted in Figure 1 with $R(g)$ replaced by the form given in Equation (3). This regularization still remains

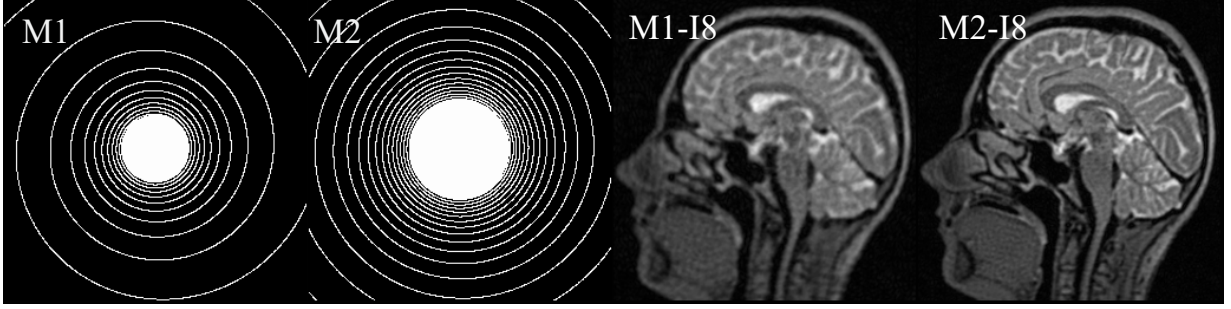


Figure 8: Spiral sampling trajectories $M_1(10\%)$ and $M_2(20\%)$, Zero filled Fourier inversions of undersampled I_8 with samples from $M_1(M_1-I_8)$ and $M_2(M_2-I_8)$.

one of the most popular and robust regularization functionals in image restoration. Lustig et. al. [3] used TV in their seminal work on undersampled MRI reconstruction.

2. Hessian-Schatten (HS) norm regularization [23]: This again belongs to the class of non-adaptive regularization depicted in Figure 1 with $R(g)$ replaced by the form given in Equation (4).
3. Total Generalized Variation (TGV) [24]: Total Generalized Variation (TGV) has been proposed as a generalization of Total Variation (TV). Only a specific form of TGV, known as second-order TGV is practicable for our problem and hence we choose this form.
4. Combined Order Regularization with Optimal Spatial Adaptation (COROSA) [42]: COROSA is a spatially weighted multi-order derivative-based regularization method for image restoration. This method has been applied to Total Internal Reflection Microscopy (TIRF) restoration and MRI reconstruction with a performance that is better than the other derivative-based regularization methods. This is the precursor of the method developed in this paper, H-COROSA.

We used a set of ten MRI images (I_1 - I_{10}) shown in Figure 7 as the reference models for comparing the proposed method with the methods listed above. We intend to study the effect of both sampling density and sampling trajectory on the performance of various reconstruction methods. For evaluating performance under variation in sampling density, we first consider a spiral sampling scheme; we used two forms of spiral with their parameters adjusted such that the trajectories cover 10% and 20% of total Fourier samples. These trajectories are given in Figure 8 with labels M_1 and M_2 . The required measurements were simulated by Fourier transforming the model images as a first step, and then picking the Fourier samples that fall in the trajectory. The spiral trajectory is an important case because it is considered to be the most efficient among other trajectories and its theoretical background is well established. To make the measurements realistic, we also simulated the effect of thermal noise in measurements by adding Additive White Gaussian Noise (AWGN) to the simulated Fourier samples [1]. The noise variance was set using the strategy of Ravishankar et. al. [18, 42], such that the noisy reconstruction from simple Fourier inversion of the full set of samples with added noise, gives a chosen Peak Signal to Noise Ratio (PSNR) value in comparison with the clean original image. We chose the PSNR to be 20dB for the measurements coming from both spiral trajectories. With two trajectories and ten model images, twenty noisy measurement sets were simulated and given as input to all reconstruction methods to be evaluated. Figure 8 also shows the inverse transform of the two sets of samples for a specific model image, where we filled in missing sample locations with zeros. Table 1 compares the reconstruction scores of the proposed methods with other regularization-based methods.

From Table 1, it is evident that H-COROSA restores resolution better than other methods, giving higher reconstruction scores. While the proposed method outperforms the compared methods in both types of sample sets, the superiority of the proposed more evident if we compare reconstructions obtained from 10% sample sets. It shows the advantage of adaptively combining the canonical second derivatives and gradients. The closest competitor to the proposed methods is COROSA, which is the pre-cursor of the proposed method. Figure 9 shows a portion of the reconstruction result of I_2 from 10% spiral samples, where H-COROSA is clearly able to restore a fine image structure that is missed by all other methods. This is evident in the corresponding scanline where a clear rise in intensity is visible in H-COROSA scanline, in alignment with the original intensity profile. Figure 10 shows a reconstructed region from I_{10} with 20% spiral samples. Again, H-COROSA reconstruction is more clear and smooth, while distortions are visible in the closest competitor, the COROSA construction. This clearly confirms the advantage of adaptively combining three terms, i.e., the advantage of combining two canonical second derivatives and the gradient. Recall that COROSA only uses two terms, namely the gradient and the norm of the Hessian. The corresponding scanline shows that H-COROSA aligns with the original intensity profile whereas the closest competitor COROSA suffers from oscillations. Figure 11 shows a

Table 1: MRI Reconstruction Scores with Spiral Trajectory: 10% and 20% Sampling Densities

I1	SSIM		SNR		I6	SSIM		SNR	
	10%	20%	10%	20%		10%	20%	10%	20%
H-COR.	.967	.983	24.57	27.94	H-COR.	.937	.983	19.39	25.51
COR.	.966	.983	24.09	28.12	COR.	.940	.985	19.71	26.12
TGV2	.959	.979	22.86	26.68	TGV2	.926	.984	18.33	25.80
TV2	.955	.972	22.07	24.71	TV2	.921	.982	18.22	25.52
HS	.955	.976	22.14	25.78	HS	.922	.982	18.32	25.57
I2	SSIM		SNR		I7	SSIM		SNR	
	10%	20%	10%	20%		10%	20%	10%	20%
H-COR.	.994	.998	25.02	30.74	H-COR.	.976	.994	31.14	37.83
COR.	.992	.998	23.58	30.45	COR.	.968	.992	29.44	36.46
TGV2	.982	.995	20.20	26.06	TGV2	.968	.994	29.08	38.20
TV2	.978	.990	18.95	22.68	TV2	.965	.994	28.98	37.99
HS	.978	.993	19.09	24.54	HS	.966	.994	29.25	38.09
I3	SSIM		SNR		I8	SSIM		SNR	
	10%	20%	10%	20%		10%	20%	10%	20%
H-COR.	.921	.968	20.98	25.17	H-COR.	.878	.942	17.42	20.91
COR.	.898	.962	19.44	24.58	COR.	.851	.937	16.73	20.98
TGV2	.879	.952	18.33	23.12	TGV2	.853	.939	16.52	20.56
TV2	.879	.940	18.00	21.50	TV2	.843	.932	16.46	20.32
HS	.882	.948	18.18	22.62	HS	.847	.934	16.60	20.48
I4	SSIM		SNR		I9	SSIM		SNR	
	10%	20%	10%	20%		10%	20%	10%	20%
H-COR.	.945	.974	20.14	24.12	H-COR.	.927	.964	18.34	22.24
COROSA	.938	.975	19.48	24.38	COR.	.921	.965	17.95	22.40
TGV2	.888	.926	18.50	22.82	TGV2	.900	.957	16.73	21.19
TV2	.922	.958	18.16	21.00	TV2	.895	.952	16.56	20.56
HS	.923	.964	18.19	21.98	HS	.896	.952	16.65	20.69
I5	SSIM		SNR		I10	SSIM		SNR	
	10%	20%	10%	20%		10%	20%	10%	20%
H-COR.	.987	.995	21.36	26.99	H-COR.	.902	.953	21.20	24.95
COR.	.986	.996	21.21	27.43	COR.	.892	.952	20.68	25.01
TGV2	.977	.984	18.62	19.96	TGV2	.886	.954	20.10	24.91
TV2	.972	.984	17.15	19.36	TV2	.880	.949	19.83	24.50
HS	.972	.987	17.18	20.98	HS	.882	.949	19.92	24.59

reconstructed portion of $I3$ where H-COROSA not only restores fine details but also has significantly reduced artifacts. The intensity profile along the selected scan line also shows that H-COROSA not only tracks the clean original intensity but also avoids oscillations. In effect, we can summarize from the first experiment that H-COROSA provides significant advantages over other state-of-the-art regularization methods in MRI reconstruction, when the sampling density is low.

Naturally, the next question is whether this advantage of H-COROSA is trajectory specific and so we consider two forms of sampling trajectories: radial trajectory given the figure 12.R1, and a form of quasi-random trajectory known as Traveling Salesman Problem (TSP) trajectory given in the Figure 12.T1. The TSP trajectory proposed by Chauffert et al [44], was inspired by the recent observation that random sampling leads to improved reconstruction [3, 14, 45–47]. As a truly random trajectory is not physically realizable, the authors constructed the trajectory given in the Figure by solving the well-known traveling salesman problem. We set the sampling density of $R1$ to 10% and $T1$ to 12%, since we are interested in performance under low sampling density. The noise variance was set such that the PSNR is 20dB, as done in the previous experiment. Figure 12 also shows the loss of details using zero-filled Fourier inversions. The evaluation scores of the reconstructions obtained by various methods from the sample set corresponding to these trajectories are given in Table 2.

Table 2 shows that H-COROSA performs better than all methods with both trajectories, with a higher improvement in score over other methods in the case of TSP sampling. This table clearly confirms that H-COROSA gives better reconstruction over other regularization methods with low sampling density, irrespective of the utilized trajectory. Figure

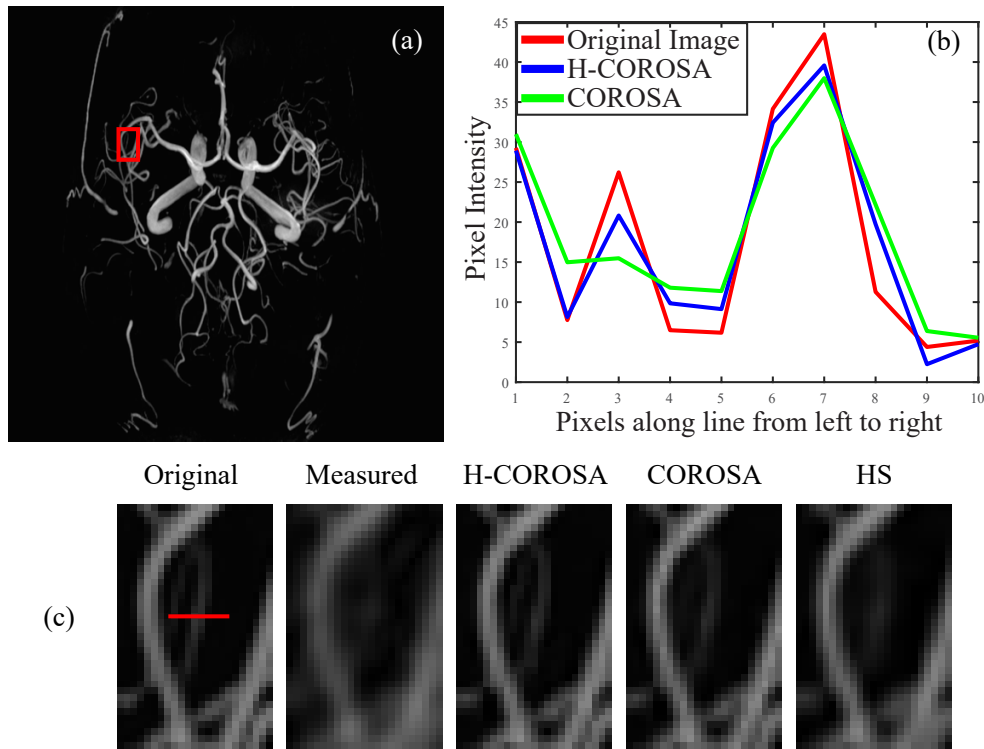


Figure 9: Reconstruction of I_2 from 10% spiral samples: (a) Original I_2 with selected region (b) Intensity profile along a scanline in the selected region (c) Comparison of selected region from reconstructions along with the scanline location. Here ‘measured’ denotes zero-filled inverse DFT of measured samples.

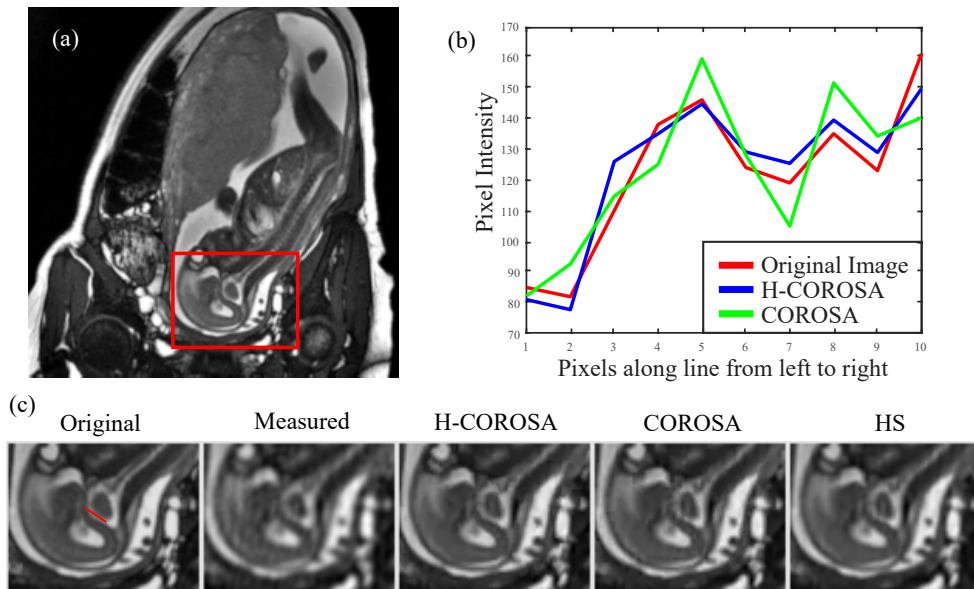


Figure 10: Reconstruction of I_{10} from 20% spiral samples: (a) Original I_{10} with selected region (b) Intensity profile along a scanline in the selected region (c) Comparison of selected region from reconstructions along with the scanline location. Here ‘measured’ denotes zero-filled inverse DFT of measured samples.

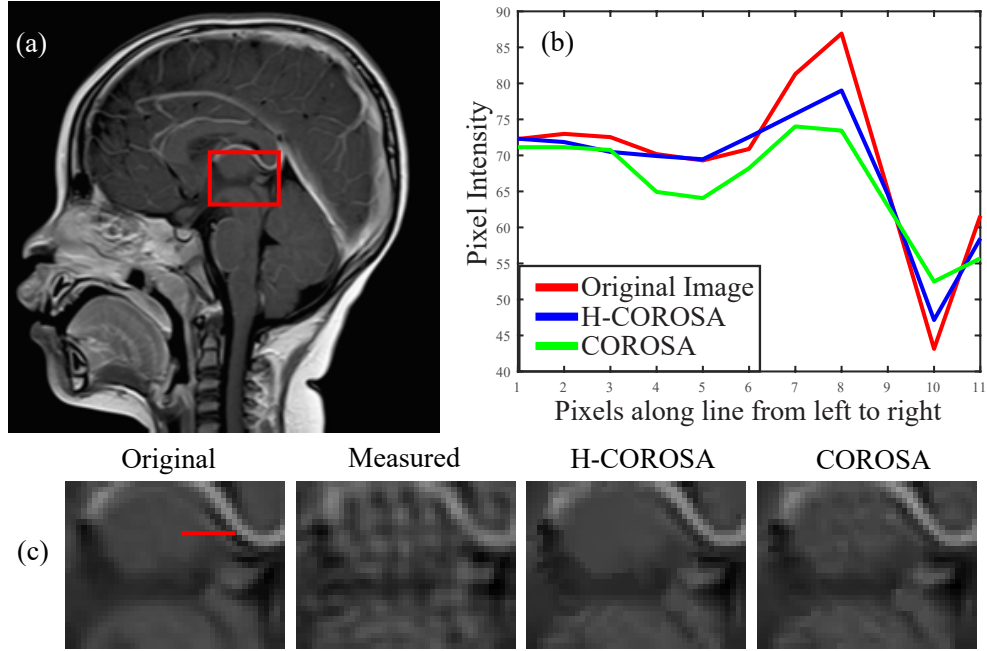


Figure 11: Reconstruction of I_3 from 20% spiral samples: (a) Original I_2 with selected region (b) Intensity profile along a scanline in the selected region (c) Comparison of selected region from reconstructions along with the scanline location. Here ‘measured’ denotes zero-filled inverse DFT of measured samples.

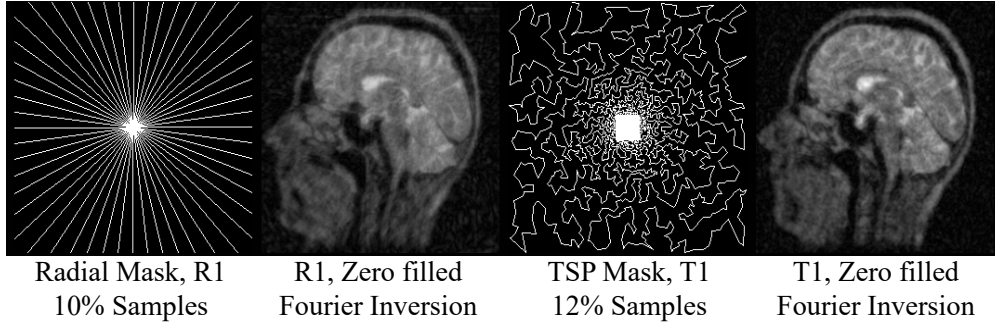


Figure 12: Radial sampling trajectory R_1 and TSP trajectory T_1 along with zero filled Fourier inversions of undersampled I_8 image with samples from corresponding trajectories.

13 shows a reconstructed region from I_8 with 12% TSP sampling, where the restoration by H-COROSA is noticeable sharper than COROSA. The corresponding scanline shows that both methods smooth out some image features on account of low sampling density and noise. However, H-COROSA is able to restore sharper details aligning better with the original intensity profile, compared to COROSA. In summary, the first set of experiments show that the proposed H-COROSA approach is able to restore image details better than all well-demonstrated regularization-based methods in the presence of under-sampling and noise. This improvement is reflected both in terms of quantitative scores (SNR and SSIM) as well as visual inspection of reconstructions, where H-COROSA is able to restore fine structures while eliminating distortions caused by undersampling and noise.

4.2 Comparison with deep learning methods

The goal of this section is to compare the proposed method with deep learning methods. Deep learning methods for image recovery use layers of the so-called convolutional neural networks (CNN), where the term “deep” signifies the stacking of several layers. Many ways of using deep CNN have been reported for image recovery. Deep CNNs have several thousands of parameters whose values need to be determined by the process known as training. There are two types of training paradigm reported in the literature:

Table 2: MRI Reconstruction: Scores with TSP and Radial Sampling

I1	SSIM		SNR		I6	SSIM		SNR	
	TSP	Rad.	TSP	Rad.		TSP	Rad.	TSP	Rad.
H-COR.	.970	.963	25.66	24.03	H-COR.	.911	.878	17.93	15.86
COR.	.968	.961	25.24	23.50	COR.	.859	.859	17.28	15.55
TGV2	.956	.946	23.33	21.42	TGV2	.838	.806	15.25	13.70
TV2	.954	.943	22.68	21.29	TV2	.844	.806	15.20	13.65
HS	.955	.944	22.84	21.43	HS	.846	.808	15.31	13.74
I2	SSIM		SNR		I7	SSIM		SNR	
	TSP	Rad.	TSP	Rad.		TSP	Rad.	TSP	Rad.
H-COR.	.997	.994	28.72	25.04	H-COR.	.965	.956	29.69	27.84
COR.	.996	.992	28.05	23.77	COR.	.949	.937	27.50	25.90
TGV2	.986	.951	22.11	17.75	TGV2	.930	.914	25.70	24.04
TV2	.983	.973	20.71	18.50	TV2	.928	.910	25.58	24.02
HS	.983	.974	20.98	18.73	HS	.933	.916	26.05	24.43
I3	SSIM		SNR		I8	SSIM		SNR	
	TSP	Rad.	TSP	Rad.		TSP	Rad.	TSP	Rad.
H-COR.	.916	.894	20.93	18.77	H-COR.	.880	.840	17.82	16.37
COR.	.886	.857	19.44	17.20	COR.	.847	.808	16.97	15.64
TGV2	.835	.747	17.78	15.04	TGV2	.823	.797	16.28	15.19
TV2	.843	.789	17.59	15.49	TV2	.822	.787	16.17	15.13
HS	.851	.798	17.97	15.76	HS	.827	.792	16.33	15.27
I4	SSIM		SNR		I9	SSIM		SNR	
	TSP	Rad.	TSP	Rad.		TSP	Rad.	TSP	Rad.
H-COR.	.958	.944	22.07	20.15	H-COR.	.932	.900	19.15	16.35
COROSA	.953	.940	21.76	19.94	COR.	.917	.885	18.28	15.54
TGV2	.930	.866	19.76	17.75	TGV2	.877	.847	16.07	13.98
TV2	.929	.910	19.37	18.22	TV2	.871	.837	15.81	13.79
HS	.930	.911	19.46	18.31	HS	.875	.841	15.99	13.98
I5	SSIM		SNR		I10	SSIM		SNR	
	TSP	Rad.	TSP	Rad.		TSP	Rad.	TSP	Rad.
H-COR.	.991	.980	23.88	19.16	H-COR.	.882	.841	20.83	18.55
COR.	.990	.979	23.89	19.18	COR.	.865	.818	20.25	17.92
TGV2	.982	.959	20.81	16.55	TGV2	.827	.772	18.84	16.56
TV2	.979	.964	19.46	16.42	TV2	.831	.770	18.60	16.35
HS	.979	.965	19.54	16.50	HS	.835	.775	18.77	16.49

Sampling scheme dependent training: In this type, training requires data containing thousands of pairs, where, each pair contains a representative measured image and the ground truth image that has generated the measurement set. From the training data, network parameters are determined through computational optimization such that the network approximately produces the ground truth image as its output from the corresponding measurement as its input. Clearly, a trained network becomes specific to the sampling scheme. If the sampling scheme is changed, the network has to be retrained even if the same class of ground truth images is involved. There is a subclass in this category of networks called Generative-Adversarial Network (GAN) architecture, where two CNNs are trained simultaneously: a generator CNN to generate the reconstruction from noisy under-sampled measurement and a discriminator CNN to determine the quality of the reconstruction. This results in a combined optimization between the two networks, towards improving the quality of reconstruction. Yang et al applied this scheme for MRI reconstruction [29], and they called the resulting network the Deep De-Aliasing Generative Adversarial Networks (DAGAN).

Plug and Play deep learning approach: This approach mimics the regularization method, where a deep CNN plays the role of regularization. However, the network does not work directly as the regularization, but indirectly as a denoising network. To be more specific, we first note that image reconstruction using derivative-based regularization is carried out by splitting-based numerical optimization methods. A splitting-based method obtains reconstruction by using computational steps involving data fitting and regularization parts independently and performs these steps cyclically until some convergence condition is attained. A crucial computational step in such schemes is denoising certain

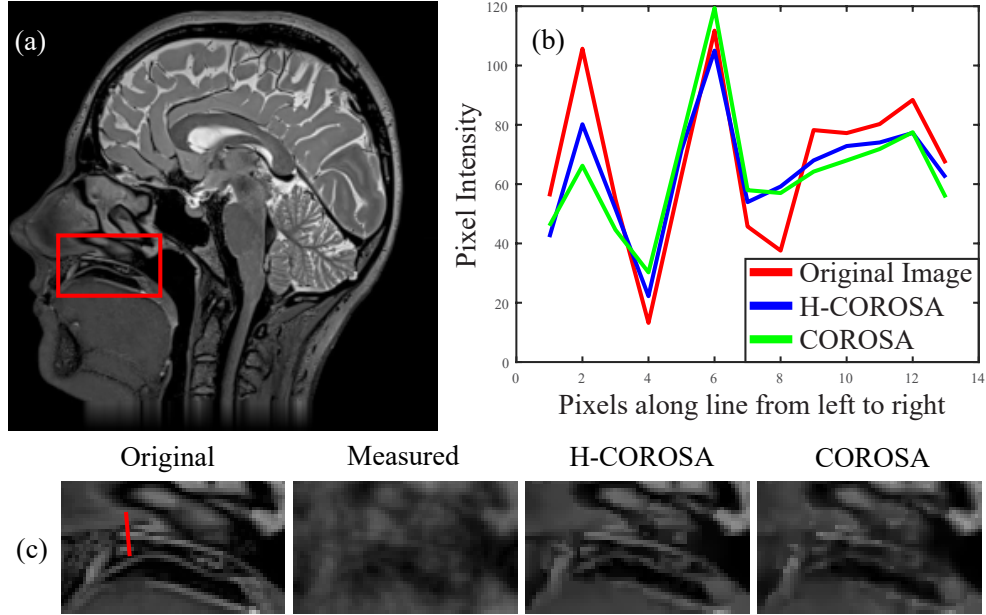
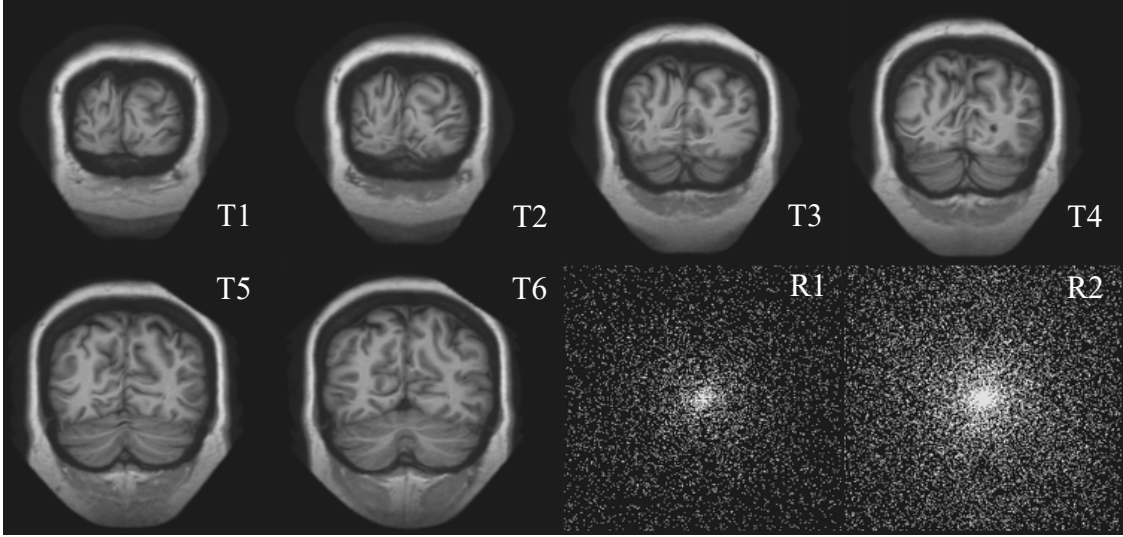


Figure 13: Reconstruction of I_8 from 12% tsp samples: (a) Original I_8 with selected region (b) Intensity profile along a scanline in the selected region (c) Comparison of selected region from reconstructions along with the scanline location. Here ‘measured’ denotes zero-filled inverse DFT of measured samples.

intermediate images using regularization. Plug and Play (PnP) deep learning methods are constructed by replacing this denoising step with deep CNN. Depending on the type of splitting-based method used as the base method, various types of PnP methods are formed. A class of PnP methods known as the ADMM-PnP method was constructed by modifying a widely used splitting method known as the Alternating Direction Method of Multipliers. In this class, the most successful one was developed by Ryu et al [48]. We select this method for our comparison. For brevity, we simply refer to this method by PnP, although there are various types of PnP methods. Note that the training here is not specific to the sampling scheme. However, the training is specific to the least-squares difference between zero-filled-in Fourier inversion of the measurement and the underlying ground truth image.

For both types of methods listed above, we make use of training data used by the authors of DAGAN [49]. We also use the recommended settings/parameters for training DAGAN network, with the code given by the authors [50]. In addition, we also include the trained networks posted by the authors of the PnP method for comparison [51]. Only the best score from these networks is updated as the reconstruction score for the PnP method. To evaluate all methods considered in this experiment, we select six images from the testing set used by the authors of DAGAN. These images are shown in Figure 14 (T1-T6). The figure also shows the two sampling schemes that we used to simulate the measurements; the first scheme with 10% sampling density is shown in the sub-figure R1 and the second with 20% sampling density is shown in the sub-figure R2. The sample locations for these schemes were selected randomly. Unlike the TSP sampling scheme used in the previous experiment which also has some randomness, the sampling schemes used here are not physically realizable. Nevertheless, this type of scheme has been used in compressive sensing literature [3], and hence we use these in order to get a perspective. The sampling schemes R1 and R2, and the test data images, T1-T6, together give 12 sample sets. We evaluate the methods under consideration using these sets without adding any noise, as well as, with noise added such that the SNR is -0.5dB for 10% sampling scheme, and -1.5dB for 20% sampling scheme with respect to zero filled Fourier inversions. This makes a total of 24 sample sets. Evaluation scores for reconstructions from all methods obtained using these sample sets without noise are given in Table 3, and the scores obtained using noisy sample sets are shown in Table 4.

Table 3 confirms that, in general, H-COROSA outperforms all methods in terms of SSIM scores, with the precursor method, COROSA being the closest competitor. In terms of SNR scores, H-COROSA again outperforms other methods in most cases with few exceptions where DAGAN and PNP have higher scores. It should be however emphasized that SNR measure is insensitive to artifacts containing artificial sharpening, while SSIM measure is more sensitive to such artifacts and hence more reliable. This means that in terms of preserving the structure of the underlying image, the method proposed in this paper, H-COROSA is always the best performing one. It can also be observed that the margins in the scores yielded by the proposed method are more significant in the case of 10% sample sets compared to the case

Figure 14: MRI Deep Learning Comparison Dataset: $T1$ - $T4$, Random masks $R1$ (10%) and $R2$ (20%)

of 20% sample sets. This means that H-COROSA can be a valuable tool when it is required to reduce the sampling density significantly. An example can be seen in Figure 15, where the best reconstruction results for $T4$ from 10% noiseless samples are shown. The H-COROSA reconstruction is clearly superior to all other methods visually, with less blurring and no spurious artifacts. On the other hand, PNP reconstructions have higher blurring while DAGAN reconstruction shows artificial structures. It may be noted that in terms of scores for this reconstruction, Table 3 shows higher SSIM score for H-COROSA, as confirmed by visual inspection. However, DAGAN and PNP have higher SNR scores, in spite of higher blurring and spurious artifacts as noted previously. The scan lines from the selected regions also show that H-COROSA follows the original intensity profile more consistently and closely, compared to the other methods. Table 4 shows that H-COROSA has higher SSIM scores over other methods in all images with both 10% and 20% sampling densities, in the presence of measurement noise. As seen in the case of noiseless samples, SNR scores of H-COROSA are insignificantly lower than competing methods, but, in terms of SSIM scores, H-COROSA is always better as claimed before. Overall, H-COROSA has the advantage of consistent and improved performance over the deep learning methods, while avoiding the requirements of appropriate training sets which are not always available.

Table 3: MRI Reconstruction: Comparison with deep learning methods for noiseless undersampling

T1	SSIM		SNR		T4	SSIM		SNR	
	10%	20%	10%	20%		10%	20%	10%	20%
H-COR.	.993	.999	29.51	38.22	H-COR.	.978	.996	25.01	33.67
COR.	.991	.999	28.61	37.82	COR.	.971	.996	23.14	32.94
DAG.	.961	.975	28.65	31.74	DAG.	.946	.962	27.20	29.27
PNP	.970	.986	29.18	33.12	PNP	.973	.986	26.61	32.02
T2	SSIM		SNR		T5	SSIM		SNR	
	10%	20%	10%	20%		10%	20%	10%	20%
H-COR.	.992	.998	28.93	37.08	H-COR.	.970	.995	23.91	32.66
COR.	.988	.998	27.21	36.62	COR.	.962	.994	22.63	31.94
DAG.	.959	.972	28.32	31.19	DAG.	.931	.959	25.61	28.96
PNP	.970	.986	28.57	32.88	PNP	.965	.985	25.46	31.42
T3	SSIM		SNR		T6	SSIM		SNR	
	10%	20%	10%	20%		10%	20%	10%	20%
H-COR.	.983	.997	26.37	35.14	H-COR.	.968	.994	23.81	31.86
COR.	.978	.997	25.00	34.59	COR.	.956	.993	22.03	31.05
DAG.	.951	.968	27.41	29.74	DAG.	.925	.955	24.62	28.48
PNP	.972	.986	27.58	32.57	PNP	.962	.985	24.41	31.14

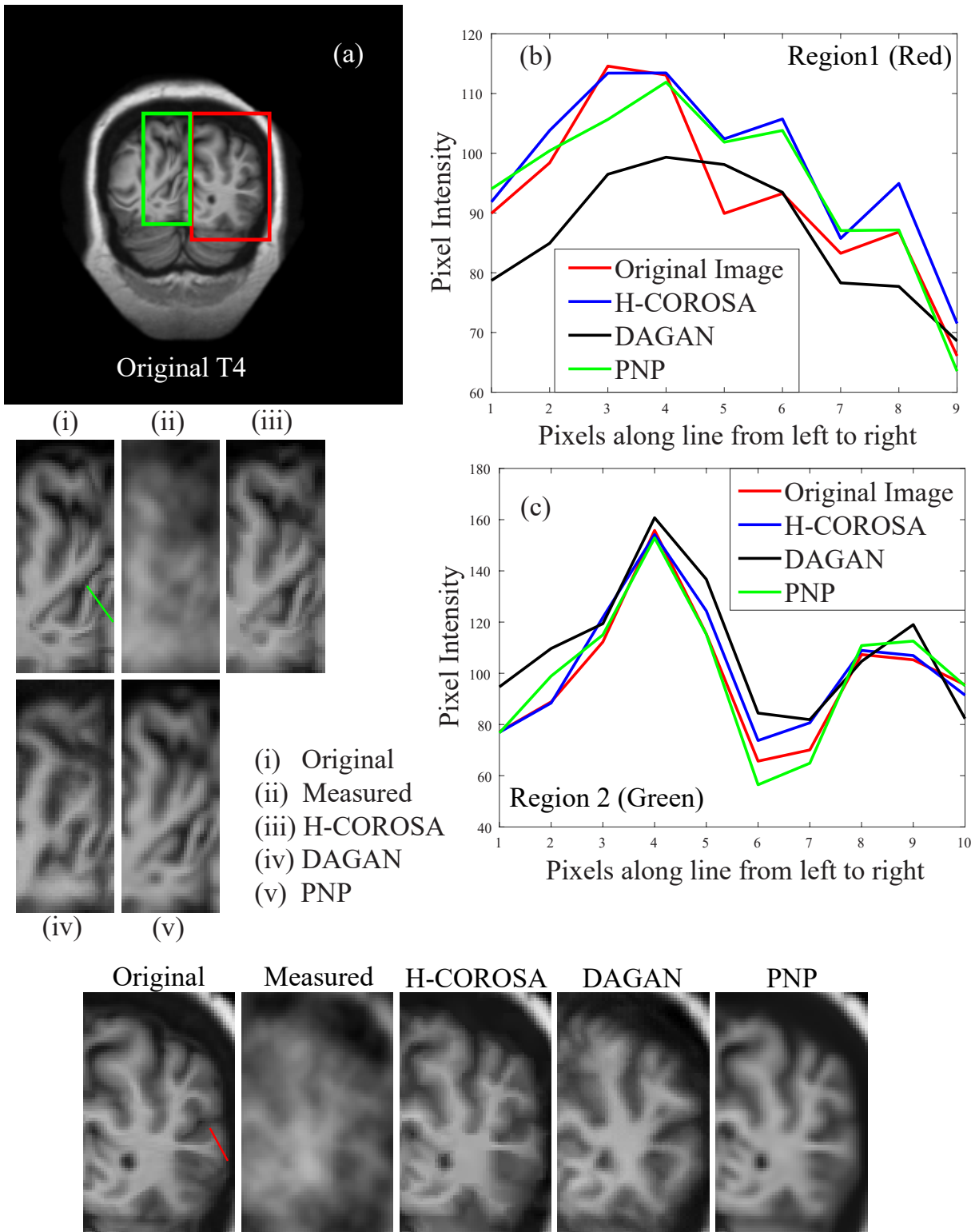


Figure 15: Reconstruction of $T4$ from 10% random noiseless samples with selected regions, scanlines and corresponding intensity profiles. Here ‘measured’ denotes zero-filled inverse DFT of measured samples.

Table 4: MRI Reconstruction: Comparison with deep learning methods for noisy samples

T1	SSIM		SNR		T4	SSIM		SNR	
	10%	20%	10%	20%		10%	20%	10%	20%
H-COR.	.924	.960	19.93	23.81	H-COR.	.904	.937	18.17	22.02
COR.	.919	.953	19.73	22.77	COR.	.898	.928	18.30	21.59
DAG.	.802	.872	18.71	24.19	DAG.	.777	.666	17.52	18.70
PNP	.807	.915	20.15	24.50	PNP	.764	.862	18.60	22.38
T2	SSIM		SNR		T5	SSIM		SNR	
	10%	20%	10%	20%		10%	20%	10%	20%
H-COR.	.917	.958	19.62	23.76	H-COR.	.901	.931	18.46	21.47
COR.	.906	.949	19.26	22.66	COR.	.887	.921	17.91	21.25
DAG.	.804	.877	18.96	24.15	DAG.	.757	.696	16.34	19.42
PNP	.777	.918	19.87	24.55	PNP	.795	.847	18.68	22.06
T3	SSIM		SNR		T6	SSIM		SNR	
	10%	20%	10%	20%		10%	20%	10%	20%
H-COR.	.915	.942	19.22	22.65	H-COR.	.891	.934	18.11	21.73
COR.	.902	.935	18.75	22.10	COR.	.877	.922	17.47	21.24
DAG.	.783	.769	17.89	21.61	DAG.	.728	.685	15.27	18.59
PNP	.783	.875	19.45	23.44	PNP	.748	.865	18.32	22.31

5 Discussion and Conclusion

In any image reconstruction problem, including the problem of reconstructing from Fourier samples, enforcing a prior model in the characteristics of the underlying image is inevitable. The quality of reconstructed images is largely determined by the suitability of the prior. Two classes of image reconstruction methods that are dominant in the current literature are the total variation (TV) regularization methods and deep learning methods. TV regularization methods rely on hand-crafted prior models that are often proven to be ad hoc leading to distortions in the reconstructed images. Deep learning methods are believed to be less distorting because they enforce natural prior derived from training, but, their need for training data is their disadvantage. Besides, concerns about some stability issues have also been raised regarding these methods [33].

The proposed regularization method, H-COROSA, which is an extension of the TV method, does not give distortions under the conditions of severe under-sampling and severe noise. It outperforms all known variants of total variation methods and well-known deep learning methods. H-COROSA can yield good quality reconstruction from highly under-sampled data. Hence it can be useful to increase the frame rate of MR imaging by setting the imaging system to scan a small fraction in the Fourier plane. Further, H-COROSA will allow improving frame rate in a wider range of studies compared to deep learning methods, because H-COROSA does not need training data. The key factor that led to the success of H-COROSA is the spatially adaptive weighting of different types of imaging derivatives. This leads to a reduction in distortions that normally occur in the non-adaptive regularizations utilizing derivatives. The key enabling factor for this adaptivity is the multiresolution scheme where the information extracted from the lower resolution reconstruction helps to improve the quality of reconstruction in the next higher resolution level.

A Overview of Derivative Based Regularization methods

The earliest form of regularization used for solving image reconstruction problems is called the Tikhonov regularization [52]. Tikhonov regularized reconstruction can be expressed as

$$s_{opt} = \underset{s}{\operatorname{argmin}} F(s, h, m) + \lambda \sum_{\mathbf{r}} \|(\mathbf{d}_1 * s)(\mathbf{r})\|_2^2 \quad (19)$$

with $d_1(\mathbf{r}) = [d_x(\mathbf{r}), d_y(\mathbf{r})]^T$,

where $d_x(\mathbf{r})$ and $d_y(\mathbf{r})$ are filters implementing first-order derivatives, $\frac{\partial}{\partial x}$, and $\frac{\partial}{\partial y}$ respectively. The above computational problem is easy to solve, but, this formulation leads to a severe loss of resolution under the noise levels ranging from moderate to high. As an improvement, the first-order total variation (TV1) [21] method was proposed, which can be

expressed as

$$s_{opt} = \underset{s}{\operatorname{argmin}} F(s, h, m) + \lambda \sum_{\mathbf{r}} \|(\mathbf{d}_1 * s)(\mathbf{r})\|_2 \quad (20)$$

The removal of squaring in the regularization leads to a better resolution and TV has been widely used [53–57] because of its ability to recover sharp image features in the presence of noise and in the cases of under-sampling. While TV1 is able to retain edges [58] in the reconstruction as compared to Tikhonov regularization [52], it presents drawbacks such as staircase artifacts [59, 60]. Higher-order extensions of TV [22, 23, 61, 62] have been proposed to avoid staircase artifacts and they deliver better restoration, albeit at the cost of increased computations. Second-order TV (TV2) [22] restoration was proposed as

$$s_{opt} = \underset{s}{\operatorname{argmin}} F(s, h, m) + \lambda \underbrace{\sum_{\mathbf{r}} \|(\mathbf{d}_2 * s)(\mathbf{r})\|_2}_{R_2(s)}, \quad (21)$$

with $\mathbf{d}_2(\mathbf{r}) = [d_{xx}(\mathbf{r}) \quad d_{yy}(\mathbf{r}) \quad \sqrt{2}d_{xy}(\mathbf{r})]^T$,

where $d_{xx}(\mathbf{r})$, $d_{yy}(\mathbf{r})$, and $d_{xy}(\mathbf{r})$ are discrete filters implementing second-order derivatives $\frac{\partial^2}{\partial x^2}$, $\frac{\partial^2}{\partial y^2}$ and $\frac{\partial^2}{\partial x \partial y}$ respectively. Another second-order derivative-based formulation is Hessian-Schatten (HS) norm regularization [23], which has been proposed as a generalization of the standard TV2 regularization. It is constructed as an ℓ_p norm of Eigenvalues of the Hessian matrix, which becomes the standard TV2 for $p = 2$. HS norm with $p = 1$ has been proven to yield the best resolution in the reconstruction since this better preserves Eigenvalues of the Hessian [23]. Let $\mathbf{H}_2(\mathbf{r})$ be the matrix filter composed of $d_{xx}(\mathbf{r})$, $d_{yy}(\mathbf{r})$, and $d_{xy}(\mathbf{r})$ and let $\zeta(\cdot)$ be the operator that returns the vector containing the Eigenvalues of its matrix argument. Then HS norm regularization of order p is expressed as

$$s_{opt} = \underset{s}{\operatorname{argmin}} F(s, h, m) + \lambda \sum_{\mathbf{r}} \|\zeta((\mathbf{H}_2 * s)(\mathbf{r}))\|_p. \quad (22)$$

Since the Eigenvalues are actually directional second derivatives taken along principle directions, setting $p = 1$ better preserves the local image structure. It has to be noted that the costs given in the equations (20), and (21) are often minimized using gradient-based approaches with smooth approximations of the form $R_k(s) = \sum_{\mathbf{r}} \sqrt{\epsilon + \|d_k(\mathbf{r}) * s(\mathbf{r})\|_2^2}$, $k = 1, 2$ where ϵ is a small positive constant [21, 63–65]. This approach has been proven to converge to the minimum of the exact form as $\epsilon \rightarrow 0$ [63]. Approaches to minimize the cost without smooth approximation include the primal-dual method [66], and alternating direction of multiplier method (ADMM) [67–70]. A detailed comparison of such approaches has been provided in [71].

It has been demonstrated that combining first- and second-order derivatives is advantageous in accurately restoring image features [24, 72–74]. In this regard, the combined order TV [73] uses scalar relative weights for combining first- and second-order variations, with the relative weights left as user parameters, and the solution is estimated by means of the optimization problem of the form

$$s_{opt} = \underset{s}{\operatorname{argmin}} F(s, h, m) + \alpha_1 R_1(s) + \alpha_2 R_2(s), \quad (23)$$

where α_1 and α_2 determine the relative weight. A generalization for total variation to higher-order terms, named total generalized variation (TGV) has also been proposed [24, 75]. It is generalized in the following ways: it is formulated for any general derivative order, and for any given order, it is generalized in the way how the derivatives are penalized. Only the second-order TGV form [24] has been well explored for image reconstruction, which takes the following form:

$$(s_{opt}, \mathbf{p}_{opt}) = \underset{s, \mathbf{p}}{\operatorname{argmin}} F(s, h, m) + \alpha_1 \sum_{\mathbf{r}} \|(\mathbf{d}_1 * s)(\mathbf{r}) - \mathbf{p}(\mathbf{r})\|_2 + \alpha_2 \frac{1}{2} \sum_{\mathbf{r}} \|\mathbf{d}_1(\mathbf{r}) * \mathbf{p}^T(\mathbf{r}) + \mathbf{p}(\mathbf{r}) * \mathbf{d}_1^T(\mathbf{r})\|_F, \quad (24)$$

where $\mathbf{p}(\mathbf{r})$ is an auxiliary 2×1 vector image. The TGV functional is able to spatially adapt to the underlying image structure because of the minimization w.r.t. auxiliary variable \mathbf{p} . Near edges, $\mathbf{p}(\mathbf{r})$ approaches zero leading to TV1-like behavior which allows sharp jumps in the edges. On the other hand, in smooth regions, $\mathbf{p}(\mathbf{r})$ approaches $\mathbf{d}_1 * s(\mathbf{r})$ leading to TV2-like behavior which will avoid staircase artifacts. However, the drawback with TGV functional is that the weights α_1 and α_2 have to be chosen by the user.

B Computation of discrete derivatives

For discrete image $s(\mathbf{r})$, discrete implementation of derivative operators $\frac{\partial}{\partial x}$, $\frac{\partial}{\partial y}$, $\frac{\partial^2}{\partial x^2}$, $\frac{\partial^2}{\partial y^2}$, and $\frac{\partial^2}{\partial x \partial y}$ are equivalent to filtering by the filters d_x , d_y , d_{xx} , d_{yy} , and d_{xy} . With $\mathbf{r} = (x, y)$, filtering with these filters can be expressed as:

$$(d_x * s)(\mathbf{r}) = s(x, y) - s(x - 1, y), \quad (25)$$

$$(d_y * s)(\mathbf{r}) = s(x, y) - s(x, y - 1), \quad (26)$$

$$(d_{xx} * s)(\mathbf{r}) = -2s(x, y) + s(x - 1, y) - s(x + 1, y), \quad (27)$$

$$(d_{yy} * s)(\mathbf{r}) = -2s(x, y) + s(x, y - 1) - s(x, y + 1), \quad (28)$$

$$(d_{xy} * s)(\mathbf{r}) = s(x, y) + s(x - 1, y - 1) - s(x - 1, y) - s(x, y - 1), \quad (29)$$

C Regularization for adaptive weight computation

Given a guide image, \hat{s} , the required adaptive weights are supposed to be the minimizer of $R(\hat{s}, \beta_1, \beta_2, \beta_2)$ with respect to weight images β_1 , β_2 , and β_2 . Recall that $R(\hat{s}, \beta_1, \beta_2, \beta_2)$ is given by

$$R(\hat{s}, \beta_1, \beta_2, \beta_2) = \sum_{\mathbf{r}} (\beta_1(\mathbf{r}) \|\nabla \hat{s}(\mathbf{r})\|_2 + \beta_2(\mathbf{r}) |\mathcal{H}^+ \hat{s}(\mathbf{r})| + \beta_3(\mathbf{r}) |\mathcal{H}^- \hat{s}(\mathbf{r})|) \quad (30)$$

Minimizing $R(\hat{s}, \beta_1, \beta_2, \beta_2)$ w.r.t. β_1 , β_2 , and β_2 subject to the conditions $0 \leq \beta_i(\mathbf{r}) \leq 1$ and $\sum_{i=1}^3 \beta_i(\mathbf{r}) = 1$ will give a solution in the following form: for each \mathbf{r} , one of $\beta_i(\mathbf{r})$ s will be 1 and others will be zeros. The value of i for which $\beta_i(\mathbf{r})$ is 1 will be the index of the element in the list $\{\|\nabla \hat{s}(\mathbf{r})\|_2, |\mathcal{H}^+ \hat{s}(\mathbf{r})|, |\mathcal{H}^- \hat{s}(\mathbf{r})|\}$ that has the lowest value. This means the adaptive weights obtained as the minimum of $R(\hat{s}, \beta_1, \beta_2, \beta_2)$ will be rapidly changing between 0 and 1 as move along the pixel indices to cope up with even insignificant differences among the terms $\{\|\nabla \hat{s}(\mathbf{r})\|_2, |\mathcal{H}^+ \hat{s}(\mathbf{r})|, |\mathcal{H}^- \hat{s}(\mathbf{r})|\}$. This will lead to artifacts in the reconstruction. Due to this reason, we determine the adaptive weights by minimizing $R(\hat{s}, \beta_1, \beta_2, \beta_2) + L(\beta_1, \beta_2, \beta_2, \tau)$ where $L(\beta_1, \beta_2, \beta_3, \tau) = -\tau \sum_{\mathbf{r}} \log(\beta_1(\mathbf{r})\beta_2(\mathbf{r})\beta_3(\mathbf{r}))$. We use the term $L(\beta_1, \beta_2, \beta_3, \tau)$ to prevent spurious changes in the values of the weights $\beta_1(\mathbf{r})$, $\beta_2(\mathbf{r})$, and $\beta_3(\mathbf{r})$. Any of the weights $\beta_1(\mathbf{r})$, $\beta_2(\mathbf{r})$, and $\beta_3(\mathbf{r})$ will approach zero only if the corresponding entry in the list is $\{\|\nabla \hat{s}(\mathbf{r})\|_2, |\mathcal{H}^+ \hat{s}(\mathbf{r})|, |\mathcal{H}^- \hat{s}(\mathbf{r})|\}$ is significantly lower than the other entries. Further, if any of the weights $\beta_1(\mathbf{r})$, $\beta_2(\mathbf{r})$, and $\beta_3(\mathbf{r})$ becomes zero, the penalty goes to ∞ . This ensures that all terms are involved at every image pixel leading to robustness against noise. The role of τ is to control the sensitivity of variations in the weight $\beta_1(\mathbf{r})$, $\beta_2(\mathbf{r})$, and $\beta_3(\mathbf{r})$ in response to the variations in the terms $\|\nabla s(\mathbf{r})\|_2$, $\mathcal{H}^+ s(\mathbf{r})$, and $\mathcal{H}^- s(\mathbf{r})$. A low value of τ imposes less penalty through $L(\beta_1, \beta_2, \beta_3, \tau)$ and hence, will promote a rapid variation in the weights $\beta_1(\mathbf{r})$, $\beta_2(\mathbf{r})$, and $\beta_3(\mathbf{r})$. Further, it will also promote the weights going close to zero. On the other hand, a high value of τ will prevent rapid variation in the weights $\beta_1(\mathbf{r})$, $\beta_2(\mathbf{r})$, and $\beta_3(\mathbf{r})$; further, it will also prevent the weights from going close to zero, and thus will make the regularization to use all three terms in a more balanced way. Hence, if τ is too high, the structural adaptivity of the regularization will be lost. This means that a balanced choice of value for τ crucial. Fortunately, we observed experimentally that a nominal value for τ that works well for various types of images and noise levels can be chosen.

D Notations and conventions for algorithm description

For a 2D discrete filter, $g(\mathbf{r})$ where $\mathbf{r} \in \mathbb{N}^2$, $g^T(\mathbf{r})$ denotes the flipped filter, i.e., $g^T(\mathbf{r}) = g(-\mathbf{r})$. The discrete convolution of the filter $g(\mathbf{r})$ with an image $x(\mathbf{r})$, denoted by $(g * x)(\mathbf{r})$, is given by $(g * x)(\mathbf{r}) = \sum_{\mathbf{t}} x(\mathbf{t})g(\mathbf{r} - \mathbf{t})$. With this, the flipped convolution will be $(g^T * x)(\mathbf{r}) = \sum_{\mathbf{t}} x(\mathbf{t})g(\mathbf{r} + \mathbf{t})$. For a vector discrete filter, $\mathbf{g}(\mathbf{r}) = [g_1(\mathbf{r}) \ g_2(\mathbf{r})]^T$, where each g_i is a discrete filter, and for an image $x(\mathbf{r})$, the notation $(\mathbf{g} * x)(\mathbf{r})$ denotes $[(g_1 * x)(\mathbf{r}) \ (g_2 * x)(\mathbf{r})]^T$, which is a vector image. For a vector image, $\mathbf{y}(\mathbf{r}) = [y_1(\mathbf{r}) \ y_2(\mathbf{r})]^T$, and a vector filter, $\mathbf{g}(\mathbf{r}) = [g_1(\mathbf{r}) \ g_2(\mathbf{r})]^T$, the notation $(\mathbf{g}^T * \mathbf{y})(\mathbf{r})$ denotes $(g_1^T * y_1)(\mathbf{r}) + (g_2^T * y_2)(\mathbf{r})$. For scalar images, $x(\mathbf{r})$ and $y(\mathbf{r})$, $(xy)(\mathbf{r})$ denotes the point-wise product, i.e., $(xy)(\mathbf{r}) = x(\mathbf{r})y(\mathbf{r})$. For a vector image $\mathbf{y}(\mathbf{r}) = [y_1(\mathbf{r}) \ y_2(\mathbf{r})]^T$ and a scalar image $z(\mathbf{r})$, the Kronocker product, $(z \oplus \mathbf{y})(\mathbf{r})$, is given by $(z \oplus \mathbf{y})(\mathbf{r}) = [(zy_1)(\mathbf{r}) \ (zy_2)(\mathbf{r})]^T$. For 3×1 vector filters and vector images, these definitions are extended in a similar way.

For a pair of images $x(\mathbf{r})$ and $y(\mathbf{r})$, we define the inner product as $\langle x, y \rangle = \sum_{\mathbf{r}} x(\mathbf{r})y(\mathbf{r})$. The norm $\|x\|_2$ is given by $\|x\|_2 = \sqrt{\langle x, x \rangle}$. For vector images, $\mathbf{x}(\mathbf{r})$ and $\mathbf{y}(\mathbf{r})$, the inner product, $\langle \mathbf{x}(\mathbf{r}), \mathbf{y}(\mathbf{r}) \rangle$ denotes $\mathbf{x}^T(\mathbf{r})\mathbf{y}(\mathbf{r})$, and $\|\mathbf{x}(\mathbf{r})\|_2$ denotes $\sqrt{\mathbf{x}^T(\mathbf{r})\mathbf{x}(\mathbf{r})}$. On the other hand, writing the same expressions without the pixel index will indicate the summation over pixel indices. In other words, we have that $\langle \mathbf{x}, \mathbf{y} \rangle = \sum_{\mathbf{r}} \mathbf{x}^T(\mathbf{r})\mathbf{y}(\mathbf{r})$, and $\|\mathbf{x}\|_2 = \sqrt{\langle \mathbf{x}, \mathbf{x} \rangle}$. The

notation $\|\mathbf{x}\|_{\cdot 2}$ denotes a scalar image that is a point-wise norm of the vector image $\mathbf{x}(\mathbf{r})$, i.e., $\|\mathbf{x}\|_{\cdot 2}(\mathbf{r}) = \sqrt{\mathbf{x}^T(\mathbf{r})\mathbf{x}(\mathbf{r})}$. With this, $\langle x, \|\mathbf{y}\|_{\cdot 2} \rangle$ will denote the sum $\sum_{\mathbf{r}} x(\mathbf{r})\|\mathbf{y}\|_{\cdot 2}(\mathbf{r})$.

We will use operators denoting the computation of Eigenvalues of a 2×2 symmetric matrices. Let $\mathbb{S}^{2 \times 2}$ denote the space of 2×2 symmetric matrices. Let $\mathbf{v} = \begin{bmatrix} v_1 & v_3 \\ v_3 & v_2 \end{bmatrix}$. We will use the notations $\Lambda_1(\mathbf{v})$ and $\Lambda_2(\mathbf{v})$ for denoting the Eigenvalues \mathbf{v} . In other words,

$$\Lambda_1(\mathbf{v}) = 0.5 \left(v_1 + v_2 + \sqrt{(v_1 - v_2)^2 + 4v_3} \right)$$

$$\Lambda_2(\mathbf{v}) = 0.5 \left(v_1 + v_2 - \sqrt{(v_1 - v_2)^2 + 4v_3} \right)$$

For a 2×2 symmetric matrix of images, \mathbf{y} , $\Lambda_1\mathbf{y}$ and $\Lambda_2\mathbf{y}$ denote the images of such Eigenvalues. For a 2×2 symmetric matrix \mathbf{v} , its Eigenvectors will be of the form $[\cos(\theta) \ \sin(\theta)]^T$, and $[-\sin(\theta) \ \cos(\theta)]^T$, where θ is the angle that depends on \mathbf{v} . Let $\Theta(\mathbf{v})$ denote the operator that returns this angle. Let $\mathcal{E}(\cdot, \cdot, \cdot)$ denote the operator that reconstructs the 2×2 symmetric matrix from the Eigenvalues and the angle determining the Eigenvectors such that $\mathbf{v} = \mathcal{E}(\Lambda_1(\mathbf{v}), \Lambda_2(\mathbf{v}), \Theta(\mathbf{v}))$.

E Adaptive regularized reconstruction with given spatial weights

The goal here is to develop the numerical algorithm for the minimizations represented by $\bar{\mathcal{M}}_{ad}^{(j)}(\cdot)$ and $\mathcal{M}_{ad}(\cdot)$ in the equations (16) and (17). Note that $\mathcal{M}_{ad}(\cdot)$ is a special case of $\bar{\mathcal{M}}_{ad}^{(j)}(\cdot)$. Specifically, we have $\bar{\mathcal{M}}_{ad}^{(0)}(\cdot) = \mathcal{M}_{ad}(\cdot)$. Hence, it is sufficient to consider $\bar{\mathcal{M}}_{ad}^{(j)}(\cdot)$. The operation represented by $\bar{\mathcal{M}}_{ad}^{(j)}(\cdot)$ is equivalent to solving the following minimization problem:

$$\begin{aligned} s^{(j)} = \operatorname{argmin}_{\substack{s = E^{(j)}\bar{s} \\ \bar{s} \in \mathbb{R}^{\frac{N}{2^j} \times \frac{N}{2^j}}}} F(s, \mathbf{m}, T) + \lambda R(s, \hat{\beta}_1, \hat{\beta}_2, \hat{\beta}_2) + \mathcal{B}(s) \end{aligned} \quad (31)$$

where

$$R(s, \hat{\beta}_1, \hat{\beta}_2, \hat{\beta}_2) = \sum_{\mathbf{r}} \left(\hat{\beta}_1(\mathbf{r}) \|\nabla s(\mathbf{r})\|_2 + \hat{\beta}_2(\mathbf{r}) |\mathcal{H}^+ s(\mathbf{r})| + \hat{\beta}_3(\mathbf{r}) |\mathcal{H}^- s(\mathbf{r})| \right), \quad (32)$$

$$F(s, \mathbf{m}, T) = \|Ts - \mathbf{m}\|_2^2, \quad (33)$$

and $\mathcal{B}(s)$ is box constraint function which takes ∞ if any of the pixels of s has a value outside a given range, and takes zero otherwise. Here the subscript lines under the argmin , $s = E^{(j)}\bar{s}$ and $\bar{s} \in \mathbb{R}^{\frac{N}{2^j} \times \frac{N}{2^j}}$ means that the optimization variable s is constrained to be of the form $s = E^{(j)}\bar{s}$ where $E^{(j)}$ is a 2^j -fold interpolator and \bar{s} is an image of size $\frac{N}{2^j} \times \frac{N}{2^j}$. Here the operator $\mathcal{H}^+ s(\mathbf{r})$ denotes computation of discrete derivatives $\frac{\partial^2}{\partial x^2}$, $\frac{\partial^2}{\partial y^2}$ and $\frac{\partial^2}{\partial x \partial y}$ and then the computation of one of the Eigenvalues of the Hessian. Similarly, $\mathcal{H}^- s(\mathbf{r})$ denotes the computation of the same set of derivatives and then the computation of the other Eigenvalue. To facilitate the development of the minimization algorithm, we have to split these notations into two stages. To this end, let $d_{xx}(\mathbf{r})$, $d_{yy}(\mathbf{r})$, and $d_{xy}(\mathbf{r})$ be discrete filters implementing second-order derivatives $\frac{\partial^2}{\partial x^2}$, $\frac{\partial^2}{\partial y^2}$ and $\frac{\partial^2}{\partial x \partial y}$ respectively, and let $\mathbf{h}(\mathbf{r}) = \begin{bmatrix} d_{xx}(\mathbf{r}) & d_{xy}(\mathbf{r}) \\ d_{xy}(\mathbf{r}) & d_{yy}(\mathbf{r}) \end{bmatrix}$. Then $(\mathbf{h} * s)(\mathbf{r})$ is 2×2 matrix of images. Then we have

$$\mathcal{H}^+ s(\mathbf{r}) = \Lambda_1((\mathbf{h} * s)(\mathbf{r})),$$

$$\mathcal{H}^- s(\mathbf{r}) = \Lambda_2((\mathbf{h} * s)(\mathbf{r})),$$

where $\Lambda_1(\cdot)$ and $\Lambda_2(\cdot)$ are the operators defined in Section D. Next, let $\mathbf{g}(\mathbf{r}) = [d_x(\mathbf{r}), d_y(\mathbf{r})]^T$ where $d_x(\mathbf{r})$ and $d_y(\mathbf{r})$ are filters implementing first order derivatives, $\frac{\partial}{\partial x}$, and $\frac{\partial}{\partial y}$ respectively. Then the adaptive regularization, $R(s, \hat{\beta}_1, \hat{\beta}_2, \hat{\beta}_3)$ can be expressed as

$$R(s, \hat{\beta}_1, \hat{\beta}_2, \hat{\beta}_3) = \sum_{\mathbf{r}} \left(\hat{\beta}_1(\mathbf{r}) \|(\mathbf{g} * s)(\mathbf{r})\|_2 + \hat{\beta}_2(\mathbf{r}) |\Lambda_1((\mathbf{h} * s)(\mathbf{r}))| + \hat{\beta}_3(\mathbf{r}) |\Lambda_2((\mathbf{h} * s)(\mathbf{r}))| \right). \quad (34)$$

Next, the constrained optimization problem of equation (31) can be written in unconstrained form by absorbing the interpolator $E^{(j)}$ into the cost function. Specifically, the cost can be written as

$$\bar{s}^{(j)} = \underset{\bar{s} \in \mathbb{R}^{\frac{N}{2^j} \times \frac{N}{2^j}}}{\operatorname{argmin}} F(E^{(j)}\bar{s}, \mathbf{m}, T) + \lambda R(E^{(j)}\bar{s}, \hat{\beta}_1, \hat{\beta}_2, \hat{\beta}_3) + \mathcal{B}(E^{(j)}\bar{s}). \quad (35)$$

Here the notations $F(E^{(j)}\bar{s}, \mathbf{m}, T)$, $R(E^{(j)}\bar{s}, \hat{\beta}_1, \hat{\beta}_2, \hat{\beta}_3)$, and $\mathcal{B}(E^{(j)}\bar{s})$ have straightforward interpretation. They represent functions obtained by replacing variable s with the 2^j -fold interpolated image $E^{(j)}\bar{s}$. We will also use the notations $F^{(j)}(\bar{s}, \mathbf{m}, T)$, $R^{(j)}(\bar{s}, \hat{\beta}_1, \hat{\beta}_2, \hat{\beta}_3)$, and $\mathcal{B}^{(j)}(\bar{s})$ to represent these functions. Note that, when $j = 0$, there is no interpolation, and hence $E^{(0)}$ denote the identity operator (the operator that returns input as the output). This means that variable \bar{s} is of original size ($N \times N$). Let $\mathcal{M}_{ad}^{(j)}(\cdot)$ denote the operator that is equivalent to the modified minimization given in the equation (35). It can be written as

$$\bar{s}^{(j)} = \mathcal{M}_{ad}^{(j)}\left(\text{OptInit} = \hat{s}, \text{AdapWt} = \{\hat{\beta}_1, \hat{\beta}_2, \hat{\beta}_3\}, \text{Data} = \{T, \mathbf{m}\}, \lambda\right). \quad (36)$$

Note that the reconstruction problems of equations (31) and (35) and nearly identical with a minor notational difference: the minimization of equation (31) searches for image s of size $N \times N$ with a constraint that $s = E^{(j)}\bar{s}$ where \bar{s} is an image of size $\frac{N}{2^j} \times \frac{N}{2^j}$. On the other hand, the minimization of equation (35) directly search for the reduced image, \bar{s} . The multiresolution loop of equation (16) can be re-expressed using the modified operator $\mathcal{M}_{ad}^{(j)}(\cdot)$ as given below:

$$\bar{s}^{(j)} = \mathcal{M}_{ad}^{(j)}\left(\text{optInit} = E^{(1)}s^{(j+1)}, \text{AdaptiveWeights} = \mathcal{M}_w\left(\text{AdaptGuide} = E^{(j+1)}s^{(j+1)}, \tau\right), \text{Data} = \{T, \mathbf{m}\}, \lambda\right) \quad (37)$$

Since the size of the minimization variable changes with the index j in modified scheme, i.e., since the size of the variable is $\frac{N}{2^j} \times \frac{N}{2^j}$, we have two changes in the multiresolution loop given above: first, the result of the previous reconstruction in the loop, $s^{(j+1)}$ goes through the 2-fold interpolation to generate initialization for numerical optimization; second, to generate adaptation guide of size $N \times N$, the result of previous reconstruction goes through a 2^{j+1} -fold interpolation.

The goal in the remainder of this section is to develop an algorithm for the minimization problem of equation (35). We use the well-known framework called the Alternating Direction Method of Multiplier (ADMM). Although the ADMM framework is well-known and frequently used for image reconstruction problems, developing an algorithm for the minimization problem of equation (35) using this framework is not a routine application and required some innovations. Our innovations are mainly in Sections E.1 and E.2.2.

E.1 Transformation of adaptive weights and constrained formulation

The first step in developing an ADMM algorithm is to re-express the optimization problem by introducing auxiliary variables related to the main variable \bar{s} through a linear equation such that each sub-cost in the problem of equation (35) can be minimized independently. This is called variable splitting. For our problem, if we extend the splitting scheme that has been used before for image reconstruction in a straightforward way, we will get the following modified problem:

$$\bar{s}^{(j)} = \underset{\bar{s}, x, \mathbf{y}, \mathbf{z}}{\operatorname{argmin}} F^{(j)}(\bar{s}, \mathbf{m}, T) + \lambda\langle\gamma, \|\mathbf{y}\|_2\rangle + \lambda\langle(1-\gamma)\zeta, |\mathbf{A}_1(\mathbf{z})|\rangle + \lambda\langle(1-\gamma)(1-\zeta), |\mathbf{A}_2(\mathbf{z})|\rangle + \mathcal{B}(x) \quad (38)$$

subject to $E^{(j)}\bar{s} = x$, $\mathbf{g} * (E^{(j)}\bar{s}) = \mathbf{y}$, and $\mathbf{h} * (E^{(j)}\bar{s}) = \mathbf{z}$. However, we observed experimentally that the algorithm derived from the above splitting leads to artifacts in the reconstruction. We propose an alternative variable splitting scheme, which is one of the main contributions of this section.

Based on our experimental observations, we present a transformation for the adaptive weights $\{\hat{\beta}_1, \hat{\beta}_2, \hat{\beta}_3\}$ that leads to faster completion of numerical optimization. Define

$$\zeta = \frac{\hat{\beta}_2}{\hat{\beta}_2 + \hat{\beta}_3} \quad (39)$$

$$\gamma = 1 - \hat{\beta}_2 - \hat{\beta}_3 \quad (40)$$

With these, $\hat{\beta}_i$'s can be expressed as

$$\hat{\beta}_1 = \gamma \quad (41)$$

$$\hat{\beta}_2 = (1-\gamma)\zeta \quad (42)$$

$$\hat{\beta}_3 = (1-\gamma)(1-\zeta) \quad (43)$$

Now the constraints $0 \leq \hat{\beta}_i \leq 1$ and $\hat{\beta}_1 + \hat{\beta}_2 + \hat{\beta}_3 = 1$ become equivalent to $0 \leq \gamma \leq 1$ and $0 \leq \zeta \leq 1$. Now consider

$$R^{(j)}(\bar{s}, \hat{\beta}_1, \hat{\beta}_2, \hat{\beta}_3) = \sum_{\mathbf{r}} \left(\hat{\beta}_1(\mathbf{r}) \|(\mathbf{g} * (E^{(j)} \bar{s}))(\mathbf{r})\|_2 + \hat{\beta}_2(\mathbf{r}) |\mathbf{\Lambda}_1((\mathbf{h} * (E^{(j)} \bar{s}))(\mathbf{r}))| + \hat{\beta}_3(\mathbf{r}) |\mathbf{\Lambda}_2((\mathbf{h} * (E^{(j)} \bar{s}))(\mathbf{r}))| \right) \quad (44)$$

Using notations introduced in Section D, the above cost can be written as

$$R^{(j)}(\bar{s}, \hat{\beta}_1, \hat{\beta}_2, \hat{\beta}_3) = \langle \beta_1, \|\mathbf{g} * (E^{(j)} \bar{s})\|_2 \rangle + \langle \beta_2, \mathbf{\Lambda}_1(\mathbf{h} * (E^{(j)} \bar{s})) \rangle + \langle \beta_3, \mathbf{\Lambda}_2(\mathbf{h} * (E^{(j)} \bar{s})) \rangle \quad (45)$$

This can be written in terms of the transformed adaptive weights as

$$R^{(j)}(\bar{s}, \gamma, \zeta) = \langle \gamma, \|\mathbf{g} * (E^{(j)} \bar{s})\|_2 \rangle + \langle \zeta(1 - \gamma), \mathbf{\Lambda}_1(\mathbf{h} * (E^{(j)} \bar{s})) \rangle + \langle (1 - \zeta)(1 - \gamma), \mathbf{\Lambda}_2(\mathbf{h} * (E^{(j)} \bar{s})) \rangle \quad (46)$$

This again can re-written as

$$R^{(j)}(\bar{s}, \gamma, \zeta) = \|\gamma \oplus (\mathbf{g} * (E^{(j)} \bar{s}))\|_2 + \langle \zeta, \mathbf{\Lambda}_1((1 - \gamma) \oplus (\mathbf{h} * (E^{(j)} \bar{s}))) \rangle + \langle (1 - \zeta), \mathbf{\Lambda}_2((1 - \gamma) \oplus (\mathbf{h} * (E^{(j)} \bar{s}))) \rangle \quad (47)$$

Now the minimization problem with updated notations can be expressed as

$$\begin{aligned} \bar{s}^{(j)} = \operatorname{argmin}_s F^{(j)}(\bar{s}, \mathbf{m}, T) + \lambda \|\gamma \oplus (\mathbf{g} * (E^{(j)} \bar{s}))\|_2 \\ + \lambda \langle \zeta, \mathbf{\Lambda}_1((1 - \gamma) \oplus (\mathbf{h} * (E^{(j)} \bar{s}))) \rangle + \lambda \langle (1 - \zeta), \mathbf{\Lambda}_2((1 - \gamma) \oplus (\mathbf{h} * (E^{(j)} \bar{s}))) \rangle + \mathcal{B}(E^{(j)} \bar{s}). \end{aligned} \quad (48)$$

The above minimization can be written as the following constrained problem,

$$\bar{s}^{(j)} = \operatorname{argmin}_{\bar{s}, x, \mathbf{y}, \mathbf{z}} F^{(j)}(s, \mathbf{m}, T) + \lambda \|\mathbf{y}\|_2 + \lambda \langle \zeta, \mathbf{\Lambda}_1(\mathbf{z}) \rangle + \lambda \langle (1 - \zeta), \mathbf{\Lambda}_2(\mathbf{z}) \rangle + \mathcal{B}(x) \quad (49)$$

subject to $E^{(j)} \bar{s} = x$, $\gamma \oplus (\mathbf{g} * (E^{(j)} \bar{s})) = \mathbf{y}$, and $(1 - \gamma) \oplus (\mathbf{h} * (E^{(j)} \bar{s})) = \mathbf{z}$.

E.2 ADMM iterations

The constrained formulation of reconstruction problem is the key for developing ADMM algorithm. The reconstruction problem is now the minimization of following cost,

$$\mathcal{J}_a(\bar{s}, x, \mathbf{y}, \mathbf{z}, \lambda) = F^{(j)}(\bar{s}, \mathbf{m}, T) + \lambda \|\mathbf{y}\|_2 + \lambda \langle \zeta, \mathbf{\Lambda}_1(\mathbf{z}) \rangle + \lambda \langle (1 - \zeta), \mathbf{\Lambda}_2(\mathbf{z}) \rangle + \mathcal{B}(x), \quad (50)$$

subject to $E^{(j)} \bar{s} = x$, $\gamma \oplus (\mathbf{g} * (E^{(j)} \bar{s})) = \mathbf{y}$, and $(1 - \gamma) \oplus (\mathbf{h} * (E^{(j)} \bar{s})) = \mathbf{z}$. The ADMM algorithm is derived through the so-called augmented Lagrangian function [76, 77]. To write augmented Lagrangian, first define

$$\begin{aligned} C(\bar{s}, x, \mathbf{y}, \mathbf{z}, \hat{x}, \hat{\mathbf{y}}, \hat{\mathbf{z}}) = \frac{c}{2} \|\gamma \oplus (\mathbf{g} * (E^{(j)} \bar{s})) - \mathbf{y}\|_2^2 + \langle \hat{\mathbf{y}}, \gamma \oplus (\mathbf{g} * (E^{(j)} \bar{s})) - \mathbf{y} \rangle \\ + c \frac{c}{2} \|(1 - \gamma) \oplus (\mathbf{h} * (E^{(j)} \bar{s})) - \mathbf{z}\|_2^2 + \langle \hat{\mathbf{z}}, (1 - \gamma) \oplus (\mathbf{h} * (E^{(j)} \bar{s})) - \mathbf{z} \rangle \\ + \frac{c}{2} \|E^{(j)} \bar{s} - x\|_2^2 + \langle \hat{x}, E^{(j)} \bar{s} - x \rangle, \end{aligned} \quad (51)$$

Here $\{\hat{x}, \hat{\mathbf{y}}, \hat{\mathbf{z}}\}$ are called the Lagrangian weights. Then the following sum is called the augmented Lagrangian:

$$L_a(\bar{s}, x, \mathbf{y}, \mathbf{z}, \hat{x}, \hat{\mathbf{y}}, \hat{\mathbf{z}}, \lambda) = \mathcal{J}_a(\bar{s}, x, \mathbf{y}, \mathbf{z}, \lambda) + C(\bar{s}, x, \mathbf{y}, \mathbf{z}, \hat{x}, \hat{\mathbf{y}}, \hat{\mathbf{z}}, \lambda) \quad (52)$$

With this definition, the ADMM method involves series of minimizations on $L_a(\bar{s}, x, \mathbf{y}, \mathbf{z}, \hat{x}, \hat{\mathbf{y}}, \hat{\mathbf{z}}, \lambda)$, where each minimization is done with respect to one of the variables in the set $\{\bar{s}, x, \mathbf{y}, \mathbf{z}\}$. Selection of the variable for minimization cycles through the list $\{\bar{s}, x, \mathbf{y}, \mathbf{z}\}$, and each cycle is considered as one step of the ADMM iteration. In other words, if k is the iteration index, the update from the current iterate denoted by $\{\bar{s}^{(k)}, x^{(k)}, \mathbf{y}^{(k)}, \mathbf{z}^{(k)}\}$, to the next iterate, $\{\bar{s}^{(k+1)}, x^{(k+1)}, \mathbf{y}^{(k+1)}, \mathbf{z}^{(k+1)}\}$ is done by the following set of minimizations and updates:

$$\mathbf{y}^{(k+1)} = \operatorname{argmin}_{\mathbf{y}} L_a(\bar{s}^{(k)}, x^{(k)}, \mathbf{y}, \mathbf{z}^{(k)}, \hat{x}^{(k)}, \hat{\mathbf{y}}^{(k)}, \hat{\mathbf{z}}^{(k)}, \lambda) \quad (53)$$

$$\mathbf{z}^{(k+1)} = \operatorname{argmin}_{\mathbf{z}} L_a(\bar{s}^{(k)}, x^{(k)}, \mathbf{y}^{(k+1)}, \mathbf{z}, \hat{x}^{(k)}, \hat{\mathbf{y}}^{(k)}, \hat{\mathbf{z}}^{(k)}, \lambda) \quad (54)$$

$$x^{(k+1)} = \operatorname{argmin}_x L_a(\bar{s}^{(k)}, x, \mathbf{y}^{(k+1)}, \mathbf{z}^{(k+1)}, \hat{x}^{(k)}, \hat{\mathbf{y}}^{(k)}, \hat{\mathbf{z}}^{(k)}, \lambda) \quad (55)$$

$$\bar{s}^{(k+1)} = \operatorname{argmin}_{\bar{s}} L_a(\bar{s}, x^{(k+1)}, \mathbf{y}^{(k+1)}, \mathbf{z}^{(k+1)}, \hat{x}^{(k)}, \hat{\mathbf{y}}^{(k)}, \hat{\mathbf{z}}^{(k)}, \lambda) \quad (56)$$

$$\hat{\mathbf{y}}^{(k+1)} = \hat{\mathbf{y}}^{(k)} + c(\gamma \oplus (\mathbf{g} * (E^{(j)} \bar{s}^{(k+1)})) - \mathbf{y}^{(k+1)}) \quad (57)$$

$$\hat{\mathbf{z}}^{(k+1)} = \hat{\mathbf{z}}^{(k)} + c((1 - \gamma) \oplus (\mathbf{h} * (E^{(j)} \bar{s}^{(k+1)})) - \mathbf{z}^{(k+1)}) \quad (58)$$

$$\hat{x}^{(k+1)} = \hat{x}^{(k)} + c(E^{(j)} \bar{s}^{(k+1)} - x^{(k+1)}) \quad (59)$$

The solution to the first and third minimizations are well-known from the literature and they can be obtained in a single step using exact formulas. We show that the solution to the second problem can be obtained in a single step and we derive the exact formula. Finally, the fourth minimization problem is a quadratic problem that can be solved iteratively using the conjugate gradient method. We will derive the computational expression for implementing the conjugate gradient iterations.

E.2.1 First minimization: the y-problem

We first rewrite the minimization problem by showing the specific terms in $L_a(\bar{s}^{(k)}, x^{(k)}, \mathbf{y}, \mathbf{z}^{(k)}, \hat{x}^{(k)}, \hat{\mathbf{y}}^{(k)}, \hat{\mathbf{z}}^{(k)}, \lambda)$ that depend on \mathbf{y} :

$$\mathbf{y}^{(k+1)} = \underset{\mathbf{y}}{\operatorname{argmin}} \lambda \|\mathbf{y}\|_2 + \frac{c}{2} \|\gamma \oplus (\mathbf{g} * (E^{(j)} \bar{s}^{(k)})) - \mathbf{y}\|_2^2 + \langle \hat{\mathbf{y}}, \gamma \oplus (\mathbf{g} * (E^{(j)} \bar{s}^{(k)})) - \mathbf{y} \rangle \quad (60)$$

The above problem is equivalent to the following problem, in which, the cost differs only by a constant independent of \mathbf{y} :

$$\mathbf{y}^{(k+1)} = \underset{\mathbf{y}}{\operatorname{argmin}} \lambda \|\mathbf{y}\|_2 + \frac{c}{2} \|\bar{\mathbf{y}}^{(k)} - \mathbf{y}\|_2^2 \quad (61)$$

where

$$\bar{\mathbf{y}}^{(k)} = |\gamma \oplus (\mathbf{g} * (E^{(j)} \bar{s}^{(k)})) + \frac{1}{c} \hat{\mathbf{y}}^{(k)} \quad (62)$$

The above minimization problem separable across pixel indices. Hence it can be written as a minimization problem in \mathbb{R}^2 as

$$\mathbf{y}^{(k+1)}(\mathbf{r}) = \underset{\mathbf{y}(\mathbf{r})}{\operatorname{argmin}} \lambda \|\mathbf{y}(\mathbf{r})\|_2 + \frac{c}{2} \|\bar{\mathbf{y}}^{(k)}(\mathbf{r}) - \mathbf{y}(\mathbf{r})\|_2^2 \quad (63)$$

The solution is well-known and is given by [78]

$$\mathbf{y}^{(k+1)}(\mathbf{r}) = \max(0, \|\bar{\mathbf{y}}^{(k)}(\mathbf{r})\| - \lambda/c) \bar{\mathbf{y}}^{(k)}(\mathbf{r}). \quad (64)$$

E.2.2 Second minimization: the z-problem

In the cost of equation (50), if ζ has a value 0.5 everywhere independent of pixel location, then the \mathbf{z} -problem can be solved using the solution derived by Lefkimmatis et al [23]. However, even if ζ does not satisfy this condition, their solution can be extended by using the same techniques used by the them, which will be the main focus of this sub-section.

Similar to how we handled the first problem, we write the second problem by showing the specific terms in $L_a(\bar{s}^{(k)}, x^{(k)}, \mathbf{y}^{(k+1)}, \mathbf{z}, \hat{x}^{(k)}, \hat{\mathbf{y}}^{(k)}, \hat{\mathbf{z}}^{(k)}, \lambda)$ that depend on \mathbf{z} :

$$\mathbf{z}^{(k+1)} = \underset{\mathbf{z}}{\operatorname{argmin}} \lambda \langle \zeta, |\mathbf{A}_1(\mathbf{z})| \rangle + \lambda \langle 1 - \zeta, |\mathbf{A}_2(\mathbf{z})| \rangle + \frac{c}{2} \|(1 - \gamma) \oplus (\mathbf{h} * (E^{(j)} \bar{s}^{(k)})) - \mathbf{z}\|_2^2 + \langle \hat{\mathbf{z}}^{(k)}, (1 - \gamma) \oplus (\mathbf{h} * (E^{(j)} \bar{s}^{(k)})) - \mathbf{z} \rangle \quad (65)$$

The equivalent minimization problem that is in the format suitable for deriving the closed-form solution is given by

$$\mathbf{z}^{(k+1)} = \underset{\mathbf{z}}{\operatorname{argmin}} \lambda \langle \zeta, |\mathbf{A}_1(\mathbf{z})| \rangle + \lambda \langle 1 - \zeta, |\mathbf{A}_2(\mathbf{z})| \rangle + \frac{c}{2} \|\bar{\mathbf{z}}^{(k)} - \mathbf{z}\|_2^2 \quad (66)$$

where

$$\bar{\mathbf{z}}^{(k)} = (1 - \gamma) \oplus (\mathbf{h} * (E^{(j)} \bar{s}^{(k)})) + \frac{1}{c} \hat{\mathbf{z}}^{(k)} \quad (67)$$

Here too, the above minimization problem is separable across pixel indices. Hence it can be written as a minimization problem in \mathbb{R}^3 as

$$\mathbf{z}^{(k+1)}(\mathbf{r}) = \underset{\mathbf{z}(\mathbf{r})}{\operatorname{argmin}} \lambda \zeta(\mathbf{r}) |\mathbf{A}_1(\mathbf{z}(\mathbf{r}))| + \lambda (1 - \zeta(\mathbf{r})) |\mathbf{A}_2(\mathbf{z}(\mathbf{r}))| + \frac{c}{2} \|\bar{\mathbf{z}}^{(k)}(\mathbf{r}) - \mathbf{z}(\mathbf{r})\|_2^2 \quad (68)$$

As mentioned before, the solution to the above problem is known for the case when $\zeta(\mathbf{r}) = 0.5$ [78], and it is not known in general. We give the solution in the following proposition.

Proposition 1. *The solution to the above problem is given by*

$$\mathbf{z}^{(k+1)}(\mathbf{r}) = \mathcal{E} \left(\mathcal{T}(\mathbf{A}_1(\bar{\mathbf{z}}^{(k+1)}(\mathbf{r})), \lambda \zeta(\mathbf{r})/c), \mathcal{T}(\mathbf{A}_2(\bar{\mathbf{z}}^{(k+1)}(\mathbf{r})), \lambda (1 - \zeta(\mathbf{r}))/c), \Theta(\bar{\mathbf{z}}^{(k+1)}(\mathbf{r})) \right),$$

where $\mathcal{T}(x, y)$ denotes soft-thresholding applied on x with threshold y , where $\mathcal{E}(\cdot)$ is the operator defined in Section D.

Proof. Let $\eta_1 = \mathbf{\Lambda}_1(\mathbf{z}(\mathbf{r}))$, $\eta_2 = \mathbf{\Lambda}_2(\mathbf{z}(\mathbf{r}))$, $\bar{\eta}_1 = \mathbf{\Lambda}_1(\bar{\mathbf{z}}^{(k+1)}(\mathbf{r}))$, and $\bar{\eta}_2 = \mathbf{\Lambda}_2(\bar{\mathbf{z}}^{(k+1)}(\mathbf{r}))$. Further, let $\theta = \Theta(\mathbf{z}(\mathbf{r}))$, $\bar{\theta} = \Theta(\bar{\mathbf{z}}^{(k+1)}(\mathbf{r}))$, where $\Theta(\cdot)$ is the operator defined in Section D. Then the minimization problem can be written as

$$(\eta_1^*, \eta_2^*, \theta^*) = \underset{\eta_1, \eta_2, \theta}{\operatorname{argmin}} \quad c_1 |\eta_1| + c_2 |\eta_2| + \frac{1}{2} \|\mathcal{E}(\eta_1, \eta_2, \theta) - \mathcal{E}(\bar{\eta}_1, \bar{\eta}_2, \bar{\theta})\|_2^2, \quad (69)$$

where $c_1 = \frac{1}{c} \lambda \zeta(\mathbf{r})$ and $c_2 = \frac{1}{c} \lambda (1 - \zeta(\mathbf{r}))$. By following the idea of Lefkimmiatis et al [23], we can conclude that the term $\frac{1}{2} \|\mathcal{E}(\eta_1, \eta_2, \theta) - \mathcal{E}(\bar{\eta}_1, \bar{\eta}_2, \bar{\theta})\|_2^2$ attains the minimum with respect to θ at $\bar{\theta}$, i.e., $\theta^* = \bar{\theta}$. At the minimum, this part of the cost becomes equal to $\frac{1}{2} (\eta_1 - \bar{\eta}_1)^2 + \frac{1}{2} (\eta_2 - \bar{\eta}_2)^2$. Hence the simplified minimization problem becomes the following:

$$(\eta_1^*, \eta_2^*) = \underset{\eta_1, \eta_2}{\operatorname{argmin}} \quad c_1 |\eta_1| + c_2 |\eta_2| + \frac{1}{2} (\eta_1 - \bar{\eta}_1)^2 + \frac{1}{2} (\eta_2 - \bar{\eta}_2)^2, \quad (70)$$

The solution is well-known and is given by [78] $\eta_1^* = \mathcal{T}(\bar{\eta}_1, c_1)$ and $\eta_2^* = \mathcal{T}(\bar{\eta}_2, c_2)$. With this, the required solution can be expressed as $\mathbf{z}^{(k+1)}(\mathbf{r}) = \mathcal{E}(n_1^*, n_2^*, \theta^*) = \mathcal{E}(\mathcal{T}(\bar{\eta}_1, c_1), \mathcal{T}(\bar{\eta}_2, c_2), \bar{\theta})$. Substituting back for $\bar{\eta}_1, \bar{\eta}_2, \bar{\theta}, c_1$ and c_2 gives final expression. \square

E.2.3 Third minimization: the x -problem

As before, we write the second problem by showing the specific terms in $L_a(\bar{s}^{(k)}, x, \mathbf{y}^{(k+1)}, \mathbf{z}^{(k+1)}, \hat{x}^{(k)}, \hat{\mathbf{y}}^{(k)}, \hat{\mathbf{z}}^{(k)}, \lambda)$ that depend on x :

$$x^{(k+1)} = \underset{x}{\operatorname{argmin}} \quad \mathcal{B}(x) + \frac{c}{2} \|E^{(j)} \bar{s}^{(k)} - x\|_2^2 + \langle \hat{x}, E^{(j)} \bar{s}^{(k)} - x \rangle \quad (71)$$

An equivalent problem is

$$x^{(k+1)} = \underset{x}{\operatorname{argmin}} \quad \mathcal{B}(x) + \frac{c}{2} \|\bar{x}^{(k)} - x\|_2^2, \quad (72)$$

where

$$\bar{x}^{(k)} = E^{(j)} \bar{s}^{(k)} + \frac{1}{c} \bar{x}^{(k)} \quad (73)$$

Again, this problem is separable across pixels, and can be written as

$$x^{(k+1)}(\mathbf{r}) = \underset{x(\mathbf{r})}{\operatorname{argmin}} \quad \mathcal{B}(x(\mathbf{r})) + \frac{c}{2} \|\bar{x}^{(k)}(\mathbf{r}) - x(\mathbf{r})\|_2^2 \quad (74)$$

The solution to this problem is well known and it is given by $x^{(k+1)}(\mathbf{r}) = \mathcal{P}(\bar{x}^{(k)}(\mathbf{r}))$, where $\mathcal{P}(\cdot)$ denotes the clipping its argument to the range within which $\mathcal{B}(x(\mathbf{r}))$ zero.

E.2.4 Fourth minimization: the s -problem

The cost $L_a(\bar{s}, x^{(k+1)}, \mathbf{y}^{(k+1)}, \mathbf{z}^{(k+1)}, \hat{x}^{(k)}, \hat{\mathbf{y}}^{(k)}, \hat{\mathbf{z}}^{(k)}, \lambda)$ with respect to \bar{s} is quadratic, and the minimum is obtained by equating the gradient of $L_a(\bar{s}, x^{(k+1)}, \mathbf{y}^{(k+1)}, \mathbf{z}^{(k+1)}, \hat{x}^{(k)}, \hat{\mathbf{y}}^{(k)}, \hat{\mathbf{z}}^{(k)}, \lambda)$ with respect s to zero. The equation is given by

$$\begin{aligned} E^{T(j)} \left(\mathbf{g}^T * \left(\gamma^2 \oplus (\mathbf{g} * (E^{(j)} \bar{s})) \right) \right) + \mathbf{h}^T * \left((1 - \gamma)^2 \oplus (\mathbf{h} * (E^{(j)} \bar{s})) \right) + b^T * b * (E^{(j)} \bar{s}) + E^{(j)} \bar{s} \\ = E^{T(j)} \left(\mathbf{g}^T * \left(\gamma^2 \oplus \tilde{\mathbf{y}}^{(k+1)} \right) \right) + \mathbf{h}^T * \left((1 - \gamma)^2 \oplus \tilde{\mathbf{z}}^{(k+1)} \right) + \tilde{x}^{(k+1)} + b^T * m, \end{aligned} \quad (75)$$

where

$$\tilde{\mathbf{y}}^{(k+1)} = \left(\mathbf{y}^{(k+1)} - \frac{1}{c} \hat{\mathbf{y}}^{(k+1)} \right) \quad (76)$$

$$\tilde{\mathbf{z}}^{(k+1)} = \left(\mathbf{z}^{(k+1)} - \frac{1}{c} \hat{\mathbf{z}}^{(k+1)} \right) \quad (77)$$

$$\tilde{x}^{(k+1)} = \left(x^{(k+1)} - \frac{1}{c} \hat{x}^{(k+1)} \right). \quad (78)$$

Here m denotes the inverse DFT of the image obtained by inserting measured samples in a 2D array of zeros. Further, b denotes inverse DFT of the binary image containing ones at locations where Fourier samples were measured and zeros at other locations. The above equation can be solved by the method of conjugate gradients.

F Computation of spatially adaptive weights

Here we consider the problem of determining the adaptive weights with the guide image $\hat{s}(\mathbf{r})$ given, which is represented by

$$(\hat{\beta}_1, \hat{\beta}_2, \hat{\beta}_3) = \mathcal{M}_w(\text{AdaptGuide} = \hat{s}, \tau) \quad (79)$$

Let $Y_1(\mathbf{r}, \hat{s}) = \|(\mathbf{g} * \hat{s})(\mathbf{r})\|_2$, $Y_2(\mathbf{r}, \hat{s}) = |\mathbf{A}_1((\mathbf{h} * \hat{s})(\mathbf{r}))|$, and $Y_3(\mathbf{r}, \hat{s}) = |\mathbf{A}_2((\mathbf{h} * \hat{s})(\mathbf{r}))|$, Now the minimization problem can be written as

$$\{\hat{\beta}_1, \hat{\beta}_2, \hat{\beta}_3\} = \underset{\beta_1, \beta_2, \beta_3}{\operatorname{argmin}} \sum_{i=1}^3 \beta_i(\mathbf{r}) Y_i(\mathbf{r}, \hat{s}) - \tau \sum_{\mathbf{r}} \log(\beta_1(\mathbf{r}) \beta_2(\mathbf{r}) \beta_3(\mathbf{r})) \quad (80)$$

subject to

$$0 \leq \beta_i(\mathbf{r}) \leq 1 \quad \text{and} \quad \sum_{i=1}^3 \beta_i(\mathbf{r}) = 1.$$

The solution to this problem is given in the following proposition.

Proposition 2. *The solution is given by $\hat{\beta}_i(\mathbf{r}) = \frac{\tau}{Y_i(\mathbf{r}, \hat{s}) + \varphi(\mathbf{r})}$ where $\varphi(\mathbf{r})$ is such that $0 \leq \hat{\beta}_i(\mathbf{r})$ and $\sum_{i=1}^3 \hat{\beta}_i(\mathbf{r}) = 1$.*

Proof. Since the minimization problem is independent of the pixel index \mathbf{r} , we simplify the notation and write the cost to be minimized as $A(\beta_1, \beta_2, \beta_3) = \sum_{i=1}^n \beta_i y_i - \tau \log(\beta_1 \beta_2 \beta_3)$. As a first step towards obtaining the solution, we ignore the bound constraint and apply Lagrange multiplier theory to handle the equality constraint [76]. The Lagrangian is given by $A_l(\beta_1, \beta_2, \beta_3) = \sum_{i=1}^n \beta_i y_i - \tau \log(\beta_1 \beta_2 \beta_3) + \varphi(\sum_{i=1}^n \beta_i - 1)$, where φ is the Lagrange's multiplier. The minimum of the constrained optimization problem can be represented by the equations $\frac{\partial}{\partial \beta_i} A_l(\beta_1, \beta_2, \beta_3) = 0$, $i = 1, 2, 3$. Representing the solution by $\hat{\beta}_i$ we get $\hat{\beta}_i = \frac{\tau}{y_i + \varphi}$. Here φ has to be determined such that the constraints $0 \leq \beta_i(\mathbf{r}) \leq 1$ and $\sum_{i=1}^3 \beta_i(\mathbf{r}) = 1$ are satisfied. Bringing back the dependence on pixel index \mathbf{r} and the dependence of Y_i on \hat{s} gives the required expression for $\hat{\beta}_i(\mathbf{r})$. \square

To determine $\varphi(\mathbf{r})$ satisfying **Proposition 2**, we note that the sum $\sum_{i=1}^3 \beta_i(\mathbf{r})$ is a monotonically decreasing function of $\varphi(\mathbf{r})$. Hence $\varphi(\mathbf{r})$ that satisfies $\sum_{i=1}^3 \beta_i(\mathbf{r}) = 1$ can be determined by binary search. To determine interval for binary search, first we note that by imposing $0 \leq \hat{\beta}_i(\mathbf{r})$, $i = 1, 2, 3$, we have a lower bound on $\varphi(\mathbf{r})$ that $\varphi(\mathbf{r}) > -\beta_m(\mathbf{r})$, where $\beta_m(\mathbf{r}) = \min\{\hat{\beta}_i(\mathbf{r}), i = 1, 2, 3\}$. To determine a more useful bound, we adopt the following strategy. Lower bound on $\varphi(\mathbf{r})$ that ensures that $\sum_{i=1}^3 \beta_i(\mathbf{r}) > 1$ can be obtained by imposing $\max(\beta_i(\mathbf{r}), i = 1, 2, 3) > 1$, which leads to the lower bound on $\varphi(\mathbf{r})$ as $\tau - Y_m(\mathbf{r}, \hat{s})$ where $Y_m(\mathbf{r}, \hat{s}) = \min(Y_i(\mathbf{r}, \hat{s}), i = 1, 2, 3)$. upper bound on $\varphi(\mathbf{r})$ that ensures that $\sum_{i=1}^3 \beta_i(\mathbf{r}) < 1$ can be obtained by imposing $\max(\beta_i(\mathbf{r}), i = 1, 2, 3) < 1/3$ which leads to upper bound on $\varphi(\mathbf{r})$ as $3\tau - Y_m(\mathbf{r}, \hat{s})$. Using these bounds, a binary search on $\varphi(\mathbf{r})$ can be done such that $\sum_{i=1}^3 \beta_i(\mathbf{r}) = 1$. Since binary search can converge very fast, we can assume that the minimization problem of equation (80) can be solved exactly, in the sense that convergence can be achieved with a tolerance that is comparable with machine precision within a reasonable amount of time.

References

- [1] E Mark Haacke, Robert W Brown, Michael R Thompson, Ramesh Venkatesan, et al. *Magnetic resonance imaging: physical principles and sequence design*, volume 82. Wiley-Liss New York:, 1999.
- [2] James G Pipe and Padmanabhan Menon. Sampling density compensation in mri: rationale and an iterative numerical solution. *Magnetic Resonance in Medicine: An Official Journal of the International Society for Magnetic Resonance in Medicine*, 41(1):179–186, 1999.
- [3] Michael Lustig, David Donoho, and John M Pauly. Sparse mri: The application of compressed sensing for rapid mr imaging. *Magnetic Resonance in Medicine: An Official Journal of the International Society for Magnetic Resonance in Medicine*, 58(6):1182–1195, 2007.
- [4] David L Donoho. Compressed sensing. *IEEE Transactions on information theory*, 52(4):1289–1306, 2006.
- [5] Emmanuel J Candès et al. Compressive sampling. In *Proceedings of the international congress of mathematicians*, volume 3, pages 1433–1452. Madrid, Spain, 2006.

- [6] Emmanuel J Candes and Terence Tao. Near-optimal signal recovery from random projections: Universal encoding strategies? *IEEE transactions on information theory*, 52(12):5406–5425, 2006.
- [7] Yaakov Tsaig and David L Donoho. Extensions of compressed sensing. *Signal processing*, 86(3):549–571, 2006.
- [8] Emmanuel J Candes and Justin Romberg. Quantitative robust uncertainty principles and optimally sparse decompositions. *Foundations of Computational Mathematics*, 6(2):227–254, 2006.
- [9] Richard G Baraniuk. Compressive sensing [lecture notes]. *IEEE signal processing magazine*, 24(4):118–121, 2007.
- [10] Michael Elad. Optimized projections for compressed sensing. *IEEE Transactions on Signal Processing*, 55(12):5695–5702, 2007.
- [11] Gabriel Peyre. Best basis compressed sensing. *IEEE Transactions on Signal Processing*, 58(5):2613–2622, 2010.
- [12] Joel A Tropp and Stephen J Wright. Computational methods for sparse solution of linear inverse problems. *Proceedings of the IEEE*, 98(6):948–958, 2010.
- [13] Marco F Duarte and Yonina C Eldar. Structured compressed sensing: From theory to applications. *IEEE Transactions on signal processing*, 59(9):4053–4085, 2011.
- [14] Emmanuel J Candès, Justin Romberg, and Terence Tao. Robust uncertainty principles: Exact signal reconstruction from highly incomplete frequency information. *IEEE Transactions on information theory*, 52(2):489–509, 2006.
- [15] Joshua Trzasko and Armando Manduca. Highly undersampled magnetic resonance image reconstruction via homotopic ℓ_0 -minimization. *IEEE Transactions on Medical imaging*, 28(1):106–121, 2008.
- [16] Shiqian Ma, Wotao Yin, Yin Zhang, and Amit Chakraborty. An efficient algorithm for compressed mr imaging using total variation and wavelets. In *2008 IEEE Conference on Computer Vision and Pattern Recognition*, pages 1–8. IEEE, 2008.
- [17] Michael Lustig, David L Donoho, Juan M Santos, and John M Pauly. Compressed sensing mri. *IEEE signal processing magazine*, 25(2):72–82, 2008.
- [18] Saiprasad Ravishankar and Yoram Bresler. MR image reconstruction from highly undersampled k-space data by dictionary learning. *IEEE transactions on medical imaging*, 30(5):1028, 2011.
- [19] Vishal M Patel, Ray Maleh, Anna C Gilbert, and Rama Chellappa. Gradient-based image recovery methods from incomplete fourier measurements. *IEEE Transactions on Image Processing*, 21(1):94–105, 2011.
- [20] Daiki Tamada and Katsumi Kose. Two-dimensional compressed sensing using the cross-sampling approach for low-field mri systems. *IEEE transactions on medical imaging*, 33(9):1905–1912, 2014.
- [21] Leonid I. Rudin, Stanley Osher, and Emad Fatemi. Nonlinear total variation based noise removal algorithms. *Physica D: Nonlinear Phenomena*, 60(1–4):259 – 268, 1992.
- [22] O. Scherzer. Denoising with higher order derivatives of bounded variation and an application to parameter estimation. *Computing*, 60(1):1–27, 1998.
- [23] S. Lefkimmiatis, J. P. Ward, and M. Unser. Hessian Schatten-norm regularization for linear inverse problems. *IEEE Transactions on Image Processing*, 22(5):1873–1888, 2013.
- [24] Florian Knoll, Kristian Bredies, Thomas Pock, and Rudolf Stollberger. Second order total generalized variation (TGV) for MRI. *Magnetic Resonance in Medicine*, 65(2):480–491, 2011.
- [25] Kyong Hwan Jin, Michael T McCann, Emmanuel Froustey, and Michael Unser. Deep convolutional neural network for inverse problems in imaging. *IEEE Transactions on Image Processing*, 26(9):4509–4522, 2017.
- [26] Jo Schlemper, Jose Caballero, Joseph V Hajnal, Anthony N Price, and Daniel Rueckert. A deep cascade of convolutional neural networks for dynamic mr image reconstruction. *IEEE transactions on Medical Imaging*, 37(2):491–503, 2017.
- [27] Kyong Hwan Jin, Michael T McCann, Emmanuel Froustey, and Michael Unser. Deep convolutional neural network for inverse problems in imaging. *IEEE Transactions on Image Processing*, 26(9):4509–4522, 2017.
- [28] Jiulong Liu, Tao Kuang, and Xiaoqun Zhang. Image reconstruction by splitting deep learning regularization from iterative inversion. In Alejandro F. Frangi, Julia A. Schnabel, Christos Davatzikos, Carlos Alberola-López, and Gabor Fichtinger, editors, *Medical Image Computing and Computer Assisted Intervention – MICCAI 2018*, pages 224–231, Cham, 2018. Springer International Publishing.
- [29] G. Yang, S. Yu, H. Dong, G. Slabaugh, P. L. Dragotti, X. Ye, F. Liu, S. Arridge, J. Keegan, Y. Guo, and D. Firmin. DAGAN: Deep de-aliasing generative adversarial networks for fast compressed sensing MRI reconstruction. *IEEE Transactions on Medical Imaging*, 37(6):1310–1321, June 2018.

- [30] Pengyue Zhang, Fusheng Wang, Wei Xu, and Yu Li. Multi-channel generative adversarial network for parallel magnetic resonance image reconstruction in k-space. In Alejandro F. Frangi, Julia A. Schnabel, Christos Davatzikos, Carlos Alberola-López, and Gabor Fichtinger, editors, *Medical Image Computing and Computer Assisted Intervention – MICCAI 2018*, pages 180–188, Cham, 2018. Springer International Publishing.
- [31] Tran Minh Quan, Thanh Nguyen-Duc, and Won-Ki Jeong. Compressed sensing mri reconstruction using a generative adversarial network with a cyclic loss. *IEEE transactions on medical imaging*, 37(6):1488–1497, 2018.
- [32] Xiaohua Zhang, Qiusheng Lian, Yuchi Yang, and Yueming Su. A deep unrolling network inspired by total variation for compressed sensing mri. *Digital Signal Processing*, 107:102856, 2020.
- [33] Vegard Antun, Francesco Renna, Clarice Poon, Ben Adcock, and Anders C. Hansen. On instabilities of deep learning in image reconstruction and the potential costs of ai. *Proceedings of the National Academy of Sciences*, 2020.
- [34] Steven Tanimoto and Theo Pavlidis. A hierarchical data structure for picture processing. *Computer graphics and image processing*, 4(2):104–119, 1975.
- [35] Hassan Ghassemian. A retina based multi-resolution image-fusion. In *IGARSS 2001. Scanning the Present and Resolving the Future. Proceedings. IEEE 2001 International Geoscience and Remote Sensing Symposium (Cat. No. 01CH37217)*, volume 2, pages 709–711. IEEE, 2001.
- [36] D.P. Huttenlocher and W.J. Rucklidge. A multi-resolution technique for comparing images using the hausdorff distance. In *Proceedings of IEEE Conference on Computer Vision and Pattern Recognition*, pages 705–706, 1993.
- [37] Haikel Salem Alhichri and Mohamed Kamel. Multi-resolution image registration using multi-class hausdorff fraction. *Pattern recognition letters*, 23(1-3):279–286, 2002.
- [38] Peter Bunting, Frédéric Labrosse, and Richard Lucas. A multi-resolution area-based technique for automatic multi-modal image registration. *Image and Vision Computing*, 28(8):1203–1219, 2010.
- [39] Byung-Gyu Kim, Jae-Ick Shim, and Dong-Jo Park. Fast image segmentation based on multi-resolution analysis and wavelets. *Pattern Recognition Letters*, 24(16):2995–3006, 2003.
- [40] Yinggan Tang, Dong Liu, and Xinping Guan. Multi-resolution image segmentation based on gaussian mixture model. *Journal of Systems Engineering and Electronics*, 17(4):870–874, 2006.
- [41] Firdaus Janoos, M Okan Irfanoglu, Kishore Mosaliganti, Raghu Machiraju, Kun Huang, Pamela Wenzel, Alain Debruin, and Gustavo Leone. Multi-resolution image segmentation using the 2-point correlation functions. In *2007 4th IEEE International Symposium on Biomedical Imaging: From Nano to Macro*, pages 300–303. IEEE, 2007.
- [42] S. Viswanath, M. Ghulyani, S. De Beco, M. Dahan, and M. Arigovindan. Image restoration by combined order regularization with optimal spatial adaptation. *IEEE Transactions on Image Processing*, 29:6315–6329, 2020.
- [43] Zhou Wang, Alan C Bovik, Hamid R Sheikh, and Eero P Simoncelli. Image quality assessment: from error visibility to structural similarity. *IEEE transactions on image processing*, 13(4):600–612, 2004.
- [44] Nicolas Chauffert, Philippe Ciuciu, Jonas Kahn, and Pierre Weiss. Variable density sampling with continuous trajectories. *SIAM Journal on Imaging Sciences*, 7(4):1962–1992, 2014.
- [45] Florian Knoll, Christian Clason, Clemens Diwok, and Rudolf Stollberger. Adapted random sampling patterns for accelerated mri. *Magnetic resonance materials in physics, biology and medicine*, 24(1):43–50, 2011.
- [46] Felix Kraher and Rachel Ward. Beyond incoherence: stable and robust sampling strategies for compressive imaging. *preprint*, 2012.
- [47] Nicolas Chauffert, Philippe Ciuciu, Jonas Kahn, and Pierre Weiss. Travelling salesman-based variable density sampling. *arXiv preprint arXiv:1307.6837*, 2013.
- [48] Ernest Ryu, Jialin Liu, Sicheng Wang, Xiaohan Chen, Zhangyang Wang, and Wotao Yin. Plug-and-play methods provably converge with properly trained denoisers. In Kamalika Chaudhuri and Ruslan Salakhutdinov, editors, *Proceedings of the 36th International Conference on Machine Learning*, volume 97 of *Proceedings of Machine Learning Research*, pages 5546–5557, Long Beach, California, USA, 09–15 Jun 2019. PMLR.
- [49] Miccai 2013 dataset, <https://my.vanderbilt.edu/masi/workshops>, .
- [50] Dagan code, <https://github.com/tensorlayer/DAGAN>, .
- [51] Provable plug and play code, https://github.com/uclaopt/Provable_Plug_and_Play, .
- [52] A. N. Tikhonov and V. Y. Arsenin. Solution of ill-posed problems. *V.H. Winston, Washington, DC*, 1977.

- [53] T. F. Chan and Chiu-Kwong Wong. Total variation blind deconvolution. *IEEE Transactions on Image Processing*, 7(3):370–375, March 1998.
- [54] I. Yanovsky, B. H. Lambrigtsen, A. B. Tanner, and L. A. Vese. Efficient deconvolution and super-resolution methods in microwave imagery. *IEEE Journal of Selected Topics in Applied Earth Observations and Remote Sensing*, 8(9):4273–4283, Sept 2015.
- [55] G. Tang and J. Ma. Application of total-variation-based curvelet shrinkage for three-dimensional seismic data denoising. *IEEE Geoscience and Remote Sensing Letters*, 8(1):103–107, Jan 2011.
- [56] Sylvain Durand and Jacques Froment. Reconstruction of wavelet coefficients using total variation minimization. *SIAM Journal on Scientific computing*, 24(5):1754–1767, 2003.
- [57] Tony F. Chan, Jianhong Shen, and Hao-Min Zhou. Total variation wavelet inpainting. *Journal of Mathematical Imaging and Vision*, 25(1):107–125, Jul 2006.
- [58] David Strong and Tony Chan. Edge-preserving and scale-dependent properties of total variation regularization. *Inverse problems*, 19(6):S165, 2003.
- [59] Wolfgang Ring. Structural properties of solutions to total variation regularization problems. *ESAIM: Mathematical Modelling and Numerical Analysis*, 34(4):799–810, 2000.
- [60] Khalid Jalalzai. Some remarks on the staircasing phenomenon in total variation-based image denoising. *Journal of Mathematical Imaging and Vision*, 54(2):256–268, Feb 2016.
- [61] Antonin Chambolle and Pierre-Louis Lions. Image recovery via total variation minimization and related problems. *Numerische Mathematik*, 76(2):167–188, 1997.
- [62] Tony Chan, Antonio Marquina, and Pep Mulet. High-order total variation-based image restoration. *SIAM Journal on Scientific Computing*, 22(2):503–516, 2000.
- [63] CR Vogel. Total variation regularization for ill-posed problems. *Report. Dept. of Mathem. Sci., Montana State Univ., USA*, 1993.
- [64] Julien Bect, Laure Blanc-Féraud, Gilles Aubert, and Antonin Chambolle. A l1-1-unified variational framework for image restoration. In *European Conference on Computer Vision*, pages 1–13. Springer, 2004.
- [65] José M Bioucas-Dias and Mário AT Figueiredo. A new twist: Two-step iterative shrinkage/thresholding algorithms for image restoration. *IEEE Transactions on Image processing*, 16(12):2992–3004, 2007.
- [66] Antonin Chambolle. An algorithm for total variation minimization and applications. *Journal of Mathematical imaging and vision*, 20(1-2):89–97, 2004.
- [67] Yilun Wang, Junfeng Yang, Wotao Yin, and Yin Zhang. A new alternating minimization algorithm for total variation image reconstruction. *SIAM Journal on Imaging Sciences*, 1(3):248–272, 2008.
- [68] M. V. Afonso, J. M. Bioucas-Dias, and M. A. T. Figueiredo. Fast image recovery using variable splitting and constrained optimization. *IEEE Transactions on Image Processing*, 19(9):2345–2356, Sep. 2010.
- [69] G. Steidl and T. Teuber. Removing multiplicative noise by Douglas-Rachford splitting methods. *Journal of Mathematical Imaging and Vision*, 36(2):168–184, Feb 2010.
- [70] M. Ghulyani and M. Arigovindan. Fast total variation based image restoration under mixed Poisson-Gaussian noise model. In *2018 IEEE 15th International Symposium on Biomedical Imaging (ISBI 2018)*, pages 1264–1267, April 2018.
- [71] Jean-François Aujol. Some first-order algorithms for total variation based image restoration. *Journal of Mathematical Imaging and Vision*, 34(3):307–327, 2009.
- [72] Marius Lysaker and Xue-Cheng Tai. Iterative image restoration combining total variation minimization and a second-order functional. *International Journal of Computer Vision*, 66(1):5–18, 2006.
- [73] K. Papafitsoros and C. B. Schönlieb. A combined first and second order variational approach for image reconstruction. *J. Math. Imaging Vision*, 48(2):308–338, 2014.
- [74] S. Viswanath, S. de Beco, M. Dahan, and M. Arigovindan. Multi-resolution based spatially adaptive multi-order total variation for image restoration. In *2018 IEEE 15th International Symposium on Biomedical Imaging (ISBI 2018)*, pages 497–500, April 2018.
- [75] Kristian Bredies, Karl Kunisch, and Thomas Pock. Total generalized variation. *SIAM Journal on Imaging Sciences*, 3(3):492–526, 2010.
- [76] Dimitri P Bertsekas. *Nonlinear programming*. Athena scientific Belmont, 1999.

- [77] Jonathan Eckstein and W Yao. Augmented Lagrangian and alternating direction methods for convex optimization: A tutorial and some illustrative computational results. *RUTCOR Research Reports*, 32:3, 2012.
- [78] Neal Parikh, Stephen Boyd, et al. Proximal algorithms. *Foundations and Trends® in Optimization*, 1(3):127–239, 2014.